



Petrogenesis and tectonic setting of late Paleoproterozoic diorites in the Trans-North China Orogen

Zhiyi Wang^{1,2}, Jun He¹, Wolfgang Siebel², Shuhao Tang¹, Yiru Ji¹, Jianfeng He¹, and Fukun Chen¹

¹State Key Laboratory of Lithospheric and Environmental Coevolution, School of Earth and Space Sciences, University of Science and Technology of China, Hefei 230026, China

²Institute of Earth and Environmental Sciences, Albert-Ludwig University Freiburg, 79104 Freiburg, Germany

Correspondence: Jun He (jhe1989@ustc.edu.cn)

Received: 7 May 2025 – Discussion started: 30 June 2025

Revised: 1 December 2025 – Accepted: 7 December 2025 – Published: 4 February 2026

Abstract. Unravelling the tectonic setting and evolution of cratons during the late Paleoproterozoic has long been a major focus of geological research. As one of Earth's major cratonic blocks, the North China Craton (NCC) preserves extensive magmatism during this period. Recent investigations have identified numerous 1.78 Ga dioritic intrusions along the southern margin and the center of the NCC. The NCC experienced widespread magmatism at ~ 1.78 Ga, and the tectonic setting of this period remains unclear and needs better understanding. Diorites of the NCC can help to constrain the late Paleoproterozoic tectonic setting in this region. In this paper we report zircon U-Pb ages of ~ 1.78 Ga and geochemical data of the Jiguanshan diorite. The diorites in the Trans-North China Orogen and the southern margin of the NCC, including the Jiguanshan diorite, have similar element and isotopic characteristics. The average initial $^{87}\text{Sr} / ^{86}\text{Sr}$ and $\varepsilon_{\text{Nd}}(t)$ values are 0.7052 ± 0.0003 and -6.5 ± 0.2 , respectively. The initial Pb isotope compositions of the diorite samples do not show significant enrichment of radiogenic lead. In terms of Sr-Nd-Pb isotope compositions and Nb / Ta, Ba / Th, and Sr / Th ratios, the diorites differ from the coeval Xiong'er volcanic rocks and mafic dike swarms. Our results suggest that the diorites originated from basaltic lower crust, rather than from enriched subcontinental lithospheric mantle. Whole-rock and zircon trace element features indicate that the diorites formed in a rift-related environment. The formation of the diorites reveals a potential transition from late Paleoproterozoic orogenic-related magmatism towards intraplate magmatism.

1 Introduction

North China Craton (NCC) was stabilized by the collision and amalgamation of several continental blocks in the late Paleoproterozoic (Fig. 1a; e.g., Zhao and Zhai, 2013; Zhao et al., 2000a, b). Subsequent widespread magmatic activity across the NCC records the cratonization process, providing critical insights into its stabilization and maturation (e.g., Zhai, 2011). The petrogenesis of the Paleoproterozoic magmatic rocks preserves key information about regional tectonic evolution and has been linked to the assembly or breakup of the Columbia supercontinent (e.g., Peng et al., 2007, 2008; Zhao et al., 2009). Among these events, the ~ 1.78 Ga magmatic event is particularly distinctive due to its large scale, leading to the production of numerous rock types including the Xiong'er volcanic rocks, A-type granites and mafic dykes (e.g., Cui et al., 2010; Hu et al., 2010; Peng et al., 2007, 2008; Wang et al., 2004; Wang et al., 2014). These rocks are extensively distributed across both the southern margin and Trans-North China Orogen of the NCC. However, the petrogenesis and tectonic setting of these rocks is debated, which revolves around post-collisional/orogenic extension (e.g., Wang et al., 2004, 2008, 2014), continental arc magmatism (e.g., He et al., 2009; Zhao et al., 2009), rifting (e.g., Cui et al., 2010; Zhao et al., 2007), and the involvement of mantle plumes (e.g., Hou et al., 2008; Peng et al., 2007, 2008). Clarifying the tectonic setting during this period is essential for understanding the geological evolution that followed the late Paleoproterozoic amalgamation of the NCC.

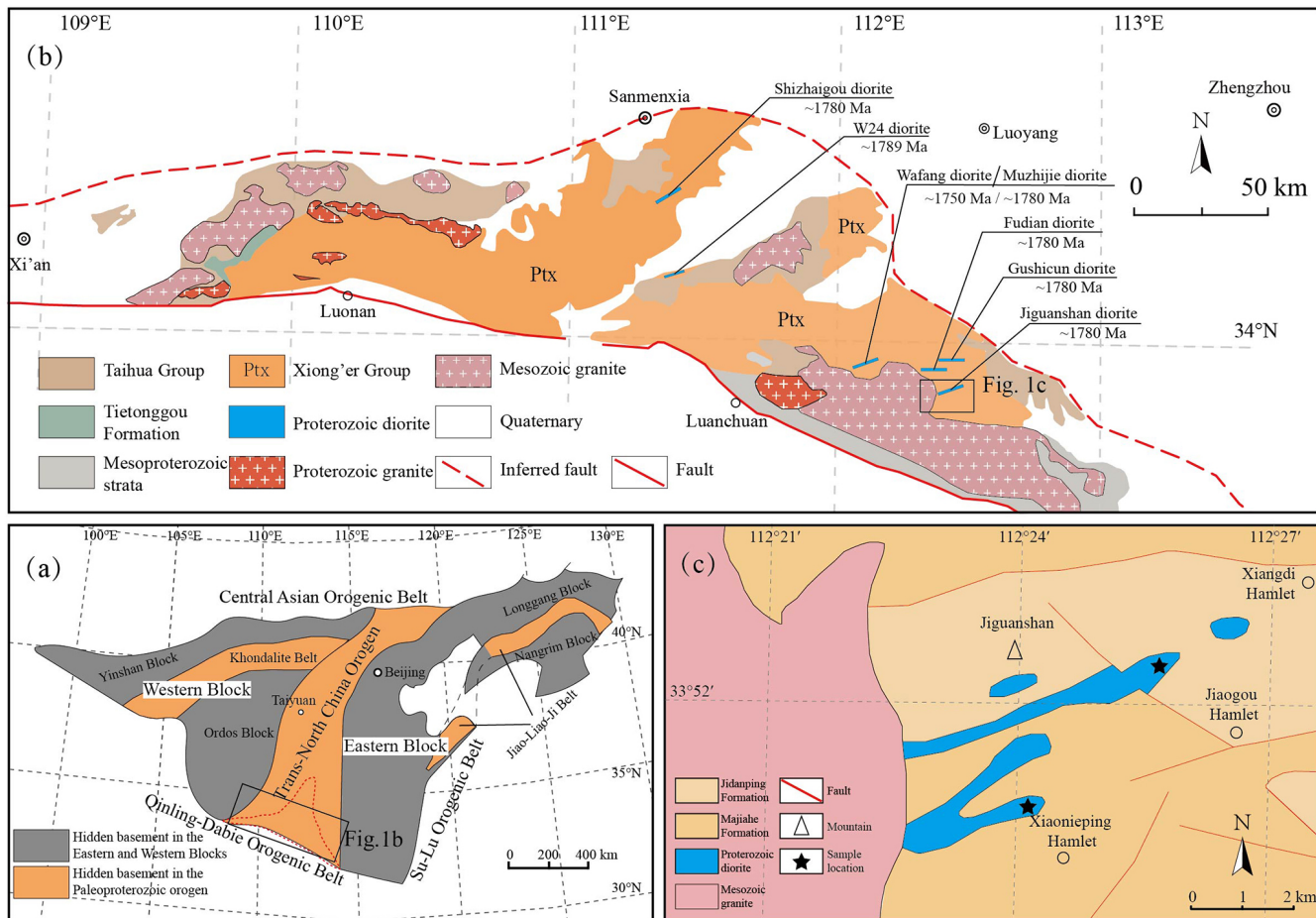


Figure 1. (a) Tectonic sketch of the North China Craton (after Zhao et al., 2001); (b) geological map of the southern margin of the North China Craton (after Diwu et al., 2014; diorites from Cui et al., 2011; Ma et al., 2023a, b; Wang et al., 2016; Zhao et al., 2004); (c) geological map of the Jiguanshan diorite (after HIGS, 2001).

In recent years, numerous diorites with ages of ca. 1780 Ma along the southern margin of the NCC and Shanxi region (Fig. 1b) have attracted significant attention, potentially offering new perspectives for understanding the tectonic evolution of the craton during the late Paleoproterozoic. These rocks include diorites intruding into Xushan Formation (at ca. 1789 Ma; Zhao et al., 2004), East-West Group dykes (ca. 1780 Ma; Peng et al., 2007), Shizhaigou diorite (ca. 1780 Ma; Cui et al., 2011), Wafang diorite (ca. 1750 Ma; Wang et al., 2016), Gushicun diorite (ca. 1780 Ma; Ma et al., 2023a), Muzhijie diorite (ca. 1780 Ma; Ma et al., 2023b), Fudian diorite (ca. 1780 Ma; Ma et al., 2023b), and Jiguanshan diorite (ca. 1780 Ma; this study). The diorites are widely distributed in an approximate east-west trending and possess similar zircon ages. Peng et al. (2007) and Cui et al. (2011) proposed that some of them share identical mantle source regions with the Xiong'er Group volcanic rocks or dyke swarms. Other authors interpret some of them resulting from fractional crystallization (Ma et al., 2023a, b) or from crustal melting with limited mantle influence (Wang et al., 2016).

Systematic research of their genesis is crucial for clarifying their formation and constraining the regional geological evolution.

The present study focuses on the Jiguanshan diorite and other diorites with ages between 1.78 and 1.75 Ga from the NCC. These diorites have similar geochemical characteristics, suggesting their formation during a single magmatic episode. By evaluating whole rock geochemical and Sr-Nd-Pb isotopic compositions, as well as Hf isotopic compositions of zircons, a better understanding of the tectonic environment and evolution of the NCC during the late Paleoproterozoic is provided.

2 Geological background and sample description

The NCC records geological evolution since 3.8 Ga ago (e.g., Geng et al., 2012; Liu et al., 1992). It consists of an Archean to Paleoproterozoic metamorphic basement lithologies overlain by Mesoproterozoic unmetamorphosed sedi-

mentary cover (e.g., Lu et al., 2008; Zhao and Zhai, 2013). The crystalline basement is composed of several microcontinental blocks (Fig. 1a; Zhao et al., 2005). Between 1.95 and 1.92 Ga, the Yinchuan and Ordos blocks collided along the Khondalite belt to form the Western Block (e.g., Li et al., 2011; Lu et al., 2008; Zhao et al., 2005). Around 1.9 Ga, the Longgang and Nangrim blocks amalgamated along the Jiao-Liao-Ji belt, forming the Eastern Block (e.g., Luo et al., 2004; Zhao et al., 2005). The NCC ultimately formed by the assembly of the Eastern and Western Blocks along the central orogenic belt at ca. 1.85 Ga (e.g., Zhao and Zhai, 2013; Zhao et al., 2000a, b, 2005). The southern margin of the NCC is separated from the North Qinling Orogen by the Luonan-Luanchuan Fault (Fig. 1b). Prior to the Mesozoic, the southern margin of the NCC has been the locus of tectonic activity. Therefore, this region is outstanding for studying the Precambrian geological evolution (e.g., Zhai, 2010).

The study area is located within the eastern part of the southern margin of the NCC (Fig. 1b). The most frequent rocks in this area are metamorphic basement rocks of the Archean Taihua Group. The Taihua Group extends in an east-west direction from Lantian in the west to Wuyang in the east (e.g., Diwu et al., 2014, 2018; Wang et al., 2020). It is primarily composed of medium- to high-grade metamorphic rocks and has been divided into the Lower and Upper Taihua Complex (e.g., Kröner et al., 1988; Shen, 1994; Wan et al., 2006; Xue et al., 1995; Zhang et al., 1985). The Lower Taihua Complex is dominated by metamorphic mafic rocks and TTG gneisses (e.g., Kröner et al., 1988; Zhang et al., 1985), whereas the Upper Taihua Complex is characterized by supracrustal sequences and metamorphic mafic rocks (e.g., Wan et al., 2006; Xue et al., 1995). Rocks of the Taihua Group record two significant stages of Archean crustal growth (e.g., Diwu et al., 2014, 2018). During the late Paleoproterozoic (1.97–1.80 Ga), the Taihua Group underwent widespread amphibolite to granulite facies metamorphism and intense deformation, reflecting collisional processes in the NCC (e.g., Diwu et al., 2018; Sun et al., 2017).

The upper part of the basement contains 1780-million-year-old volcanic rocks of the Xiong'er Group (e.g., Zhao et al., 2004, 2007). The Xiong'er volcanic rocks consist mainly of basalts and andesites that are widely distributed along the southern margin of the NCC, and extend as far north as Taiyuan City in Shanxi Province (Zhao et al., 2007). The Xiong'er Group represents the largest magmatic unit of the NCC since the Neoarchean period. At the same time, a large mafic dyke swarm intruded into the NCC. These mafic rocks are interpreted as products of crustal extension during the Columbia supercontinent era (e.g., Hou et al., 2008; Peng et al., 2008).

During fieldwork, seven diorite samples were collected from the Jiguanshan diorite on the eastern side of the Jiguanshan hill (or the Jiguan Mountain), about 30 km south of Ruyang County, Henan Province (Fig. 1c and Table S1). The Jiguanshan diorite forms several east-west striking bod-

ies that are cut by the Mesozoic Taishanmiao A-type granite to the west. The Taishanmiao intrusion covers an area of ca. 290 km² (e.g., He et al., 2021). The northern and eastern part of the Taishanmiao intrusion penetrates the volcanic rocks of the Xiong'er Group (Fig. 1c).

The collected rock samples of the Jiguanshan diorite are fresh and greyish with massive textures (Fig. 2a). They are fine-grained with grain sizes between 0.1–2 mm (Fig. 2b). The main mineral is plagioclase (~60 vol %), with lamellar or euhedral shape and variable grain size. Under the microscope, the partially sericitized crystals show simple contact twinning and polysynthetic twinning. Some plagioclase crystals show zonal and resorption textures (Fig. 2c–e) and Carlsbad-albite twinning (Fig. 2d). Clinopyroxene (~15 vol %) formed earlier than plagioclase. Most of the clinopyroxenes have zonal texture (Fig. 2f). Euhedral opaque minerals (~3 vol %), such as ilmenite, are often enclosed in clinopyroxene. Alkali-feldspar (~10 vol %) shows hypidiomorphic to xenomorphic texture with imprints of kaolinization (Fig. 2c, e). The mineral occurs as K-feldspar and perthite. Quartz (~5 vol %) occurs as an anhedral crystal. Biotite (~3 vol %) shows xenomorphic texture or is altered into chloride (Fig. 2c, e). In addition, accessory minerals such as zircon and ilmenite account for about 3 vol % (Fig. 2f).

3 Analytical methods

Whole rock major and elements: Seven fresh rock samples were grinded into powders to less than 200 mesh size. Major element composition of whole-rock samples was analyzed by X-ray fluorescence (XRF) at ALS Chemex (Guangzhou) by using PANalytical PW2424 instrument. Trace element concentrations were determined using Agilent 7700 inductively coupled plasma mass spectrometry (ICP-MS) at the University of Science and Technology of China (USTC). Measured concentrations of the reference materials (GSR-1, BCR-2, and AGV-2) are within 10 % of their recommended values and the analytical uncertainties are better than 5 %.

Whole-rock Sr-Nd-Pb isotopes: Whole-rock Sr-Nd-Pb isotope analysis was performed in the Laboratory of Radiogenic Isotope Geochemistry, USTC. ca. 100 mg whole-rock powders were decomposed in purified HF and HNO₃ acid solution for Pb isotopic analysis and purified HF and HClO₄ acid solution for Sr-Nd isotopic analysis. Sr and Nd were separated by an AG 50W-X12 resin (200–400 mesh size) and purified using the Sr-Spec® ion-exchange resin for Sr and LN-Spec® resin for Nd. All isotopic measurements were measured on a Triton Plus mass spectrometer of Thermo Scientific™. Sr and Nd ratios were normalized to ⁸⁶Sr / ⁸⁸Sr = 0.1194 and ¹⁴³Nd / ¹⁴⁴Nd = 0.7219, respectively. Pb isotope ratios were corrected for mass fractionation using a fractionation factor of 0.1 % per atomic mass unit based on repeated measurements of reference material

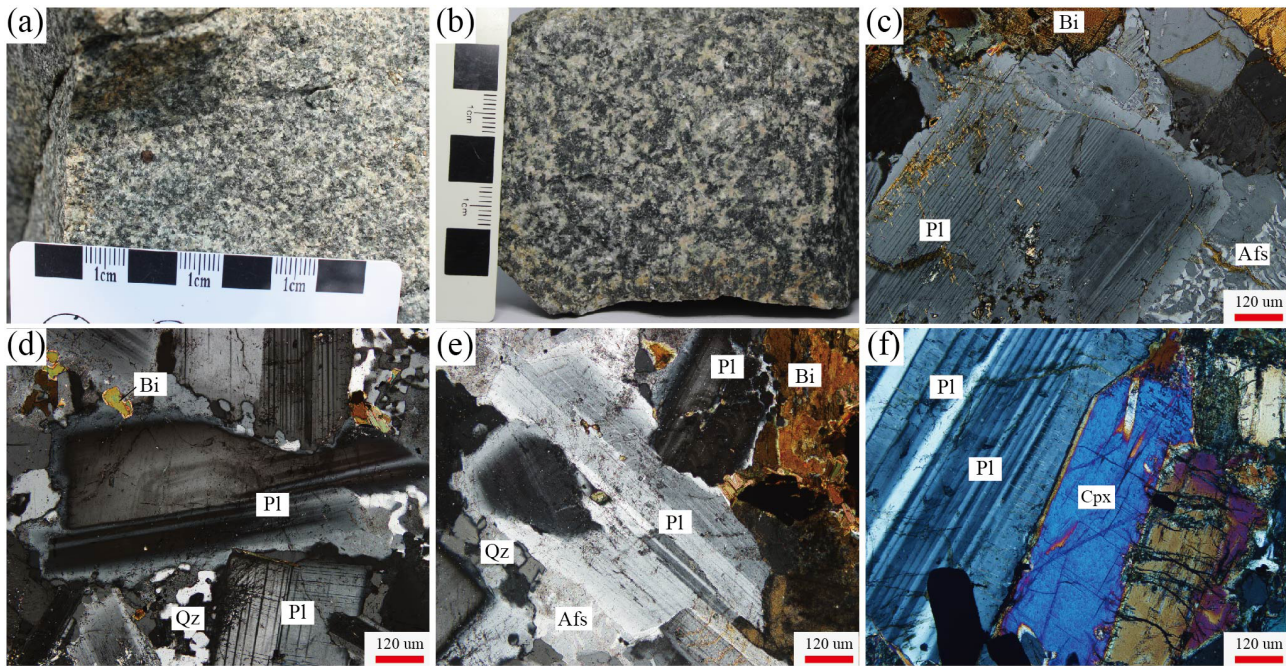


Figure 2. (a–b) Field photographs and representative hand specimens of the Jiguanshan diorite; (c–f) Microphotographs under plane-polarized light of the Jiguanshan diorite. Mineral abbreviations: Afs, alkali feldspar; Bi, biotite; Cpx, Clinopyroxene; Pl, plagioclase; Qz, quartz.

NIST NBS 981 (Wang et al., 2023b). Total procedure blanks for Sr, Nd, and Pb were less than 200 pg. Detailed analytical procedures were described in Chen et al. (2000, 2007). Errors for the initial Sr and Nd isotope ratios were obtained by the error transfer formula, which is shown in Table 2 for Sr and Table 3 for Nd. Detailed formulas can be found in Siebel et al. (2005). A 5 % age error, a 2 ‰ $^{87}\text{Rb} / ^{86}\text{Sr}$ measurement error, and a 0.3 ‰ $^{87}\text{Sr} / ^{86}\text{Sr}$ measurement error were used as uncertainties for the initial Sr value calculation. A 5 % age error, a 0.3 ‰ $^{147}\text{Sm} / ^{143}\text{Nd}$ error, and the $^{143}\text{Nd} / ^{144}\text{Nd}$ measurement error were used for calculating the initial Nd isotope uncertainty.

Zircon U-Pb geochronology and trace element composition: Zircon crystals were separated from the rock samples by standard mineral separation procedures. Grains with intact crystal shape and no obvious inclusions were selected and embedded in epoxy resin under a binocular microscope. Most of the zircon gains were polished to half to two thirds of their original thickness and then cleaned in ultra-pure water by ultrasonic waves. Cathodoluminescence (CL) image analysis was done on a scanning electron microscope (SEM) at the USTC. Zircon U-Pb isotopic and trace element compositions were obtained by laser-ablation inductively-coupled plasma mass spectrometry (LA-ICP-MS) at the USTC. The beam spot diameter was 32 μm , operating at a repetition rate of 10 Hz. Helium served as the carrier gas. Zircon 91500 was used as a standard for age calculation. The NIST SRM 610 and 612 were utilized as reference materials for element con-

tent adjustment. U-Pb ratios and uranium and lead concentration data were calculated by the ICPMSDataCal software (Liu et al., 2010). Concordia and weighted mean age plots were made using IsoplotR (Vermeesch, 2018).

4 Analytical results

Whole-rock compositions of the Jiguanshan diorite are given in Table 1, and Sr-Nd-Pb isotope compositions and error calculations are shown in Tables 2 to 4. Age results of zircon grains from four samples are given in Table S1, zircon trace element composition in Table S2.

4.1 Zircon U-Pb isotopic ages

Zircon grains from the Jiguanshan diorite are transparent to pale yellow with subhedral to euhedral habitus. They measure ca. 100–300 μm in length and have aspect ratios between 1 : 1 and 3 : 1. Most of them show oscillatory zoning in the CL images (Fig. 3), which suggests a magmatic origin.

Twenty-nine zircon grains from sample ZY2202 yield $^{207}\text{Pb} / ^{206}\text{Pb}$ ages varying from 1885 ± 44 Ma to 1643 ± 42 Ma giving a weighted mean age of 1772 ± 16 Ma (2σ , $n = 29$, MSWD = 2.2, Fig. 4a). Thirty-two zircon grains from sample ZY2204 yield $^{207}\text{Pb} / ^{206}\text{Pb}$ ages varying from 1902 ± 54 Ma to 1635 ± 47 Ma with a weighted mean age of 1742 ± 15 Ma (2σ , $n = 32$, MSWD = 1.6, Fig. 4b). Twenty-six out of twenty-seven zircon grains

Table 1. Major (wt %) and trace element contents (ppm) of the Jiguanshan diorite.

Sample No.	ZY2201	ZY2202	ZY2203	ZY2204	ZY2205	ZY2206	ZY2207
(wt %)							
SiO ₂	58.18	59.44	59.13	58.24	56.26	56.01	55.57
TiO ₂	1.87	1.37	1.36	1.82	2.01	1.87	2.05
Al ₂ O ₃	14.38	14.37	14.24	14.11	14.18	15.00	14.41
<i>T</i> Fe ₂ O ₃	10.38	9.04	9.17	10.00	10.35	10.18	10.50
MnO	0.15	0.14	0.14	0.14	0.17	0.14	0.15
MgO	2.73	2.81	2.96	2.59	2.70	2.92	2.94
CaO	5.85	5.29	5.33	5.60	5.61	6.06	5.81
Na ₂ O	2.76	2.85	2.87	2.79	2.56	2.60	2.56
K ₂ O	2.98	3.15	3.16	3.11	3.21	2.97	3.01
P ₂ O ₅	0.71	0.46	0.45	0.65	0.73	0.68	0.76
LOI	0.48	1.31	0.67	0.36	1.53	1.60	1.67
Total	100.47	100.23	99.48	99.41	99.31	100.03	99.43
(ppm)							
Li	11.2	19.8	19.9	14.8	18.6	20.7	18.2
Be	2.66	2.80	2.76	2.94	3.06	2.70	2.97
Sc	22.7	20.1	20.4	23.3	24.3	24.0	23.8
V	163	141	147	168	179	165	164
Cr	72.1	91.3	101.3	69.5	68.6	78.6	83.5
Ni	21.3	22.3	24.0	20.7	19.2	20.2	21.6
Cu	20.8	19.8	19.9	20.9	27.0	22.2	23.3
Zn	131	128	122	133	148	139	141
Ga	21.9	21.9	21.8	22.9	23.3	23.8	22.7
Rb	80.3	95.2	97.8	88.4	88.0	89.5	88.9
Sr	412	374	384	406	403	542	490
Y	47.5	44.4	43.8	48.4	49.3	44.8	46.7
Zr	402	478	474	435	428	400	407
Nb	20.2	21.2	21.0	21.2	22.7	20.3	21.8
Cs	0.60	0.77	0.74	0.95	2.98	3.63	4.44
Ba	1543	1515	1504	1544	1814	1714	1737
La	72.2	79.0	79.5	75.0	77.3	71.7	75.2
Ce	149	161	161	154	163	150	159
Pr	17.6	18.3	18.1	18.2	19.4	18.0	18.9
Nd	72.3	71.2	70.9	73.2	80.0	72.9	77.1
Sm	12.7	12.1	12.0	12.7	14.0	12.8	13.4
Eu	2.63	2.21	2.18	2.59	2.93	2.78	2.87
Gd	12.1	11.2	11.2	12.1	13.0	11.7	12.5
Tb	1.53	1.39	1.40	1.51	1.63	1.47	1.56
Dy	8.99	8.32	8.11	8.92	9.50	8.53	9.00
Ho	1.67	1.54	1.53	1.67	1.75	1.53	1.65
Er	4.97	4.56	4.54	4.95	5.09	4.55	4.87
Tm	0.62	0.55	0.55	0.60	0.63	0.55	0.58
Yb	4.26	3.79	3.84	4.18	4.33	3.82	3.99
Lu	0.61	0.55	0.56	0.60	0.63	0.55	0.58
Hf	7.97	9.09	9.15	8.20	8.46	7.59	7.98
Ta	1.03	0.98	0.99	1.01	1.10	0.96	1.07
Pb	16.4	21.2	18.0	16.3	18.9	15.2	14.2
Th	4.28	6.43	6.71	4.27	3.87	3.22	3.55
U	0.70	0.98	0.88	0.71	0.75	0.61	0.68
K ₂ O / Na ₂ O	1.08	1.11	1.10	1.11	1.25	1.14	1.18
K ₂ O + Na ₂ O (wt %)	5.74	6.00	6.03	5.90	5.77	5.57	5.57
Mg#	34.5	38.3	39.2	34.1	34.3	36.5	35.9
A / CNK	0.78	0.81	0.80	0.78	0.79	0.81	0.80
A / NK	1.85	1.77	1.75	1.77	1.84	2.00	1.93
ΣREE	361.5	375.8	375.1	370.4	393.2	361.2	381.3
Eu / Eu*	0.64	0.57	0.57	0.63	0.65	0.68	0.66
(La / Yb) _N	12.2	15.0	14.8	12.9	12.8	13.5	13.5

$$\text{Mg}^{\#} = (\text{MgO} + \text{FeO}_{\text{total}}) / \text{MgO} \times 100$$

$$\text{Eu} / \text{Eu}^* = 2\text{Eu}_{\text{N}} / (\text{Sm}_{\text{N}} + \text{Gd}_{\text{N}}); (\text{La} / \text{Yb})_{\text{N}} = \text{chondrite-normalized La} / \text{Yb ratio}.$$

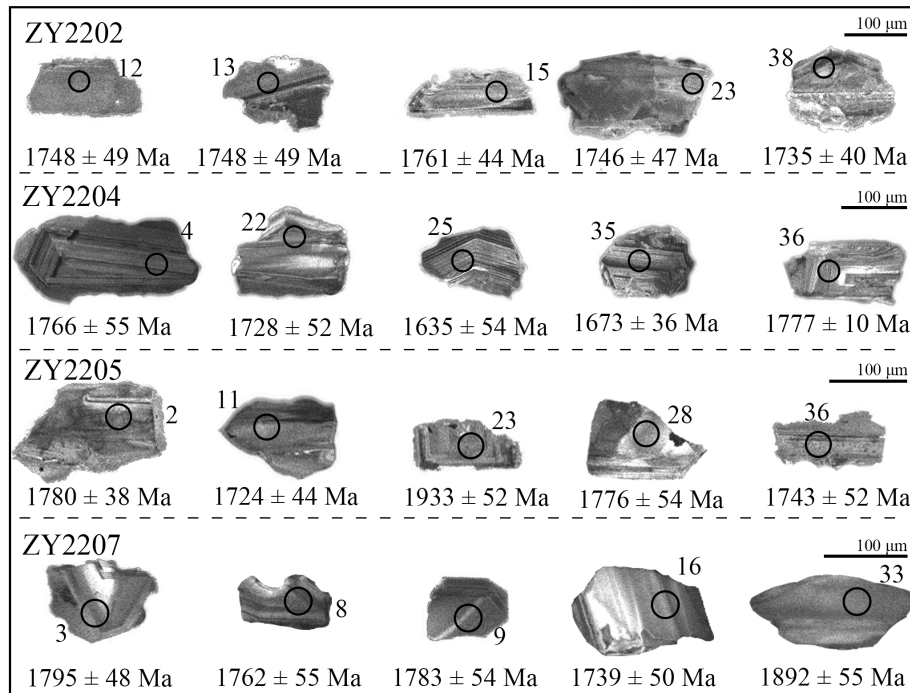


Figure 3. Cathodoluminescence (CL) images of representative zircon grains from the Jiguanshan diorite.

from sample ZY2205 yield $^{207}\text{Pb} / ^{206}\text{Pb}$ ages varying from 1933 ± 52 Ma to 1692 ± 44 Ma and a weighted mean age of 1760 ± 18 Ma (2σ , $n = 26$, $\text{MSWD} = 0.66$, Fig. 4c). One zircon with a $^{207}\text{Pb} / ^{206}\text{Pb}$ age of 1639 ± 46 Ma (96 % concordance) was excluded from the calculation after being identified as a statistical outlier by the IsoplotR program (Fig. 4c). The limited number of zircon grains of this age precludes a robust geological interpretation. Thirty zircon grains of sample ZY2207 yield $^{207}\text{Pb} / ^{206}\text{Pb}$ ages ranging from 1900 ± 54 Ma to 1700 ± 36 Ma with a weighted mean age of 1771 ± 17 Ma (2σ , $n = 30$, $\text{MSWD} = 1$, Fig. 4d).

Most zircon grains have Th / U ratios > 1 , supporting their magmatic origin (Table S1). Some grains deviate from the Concordia curve, which is related to lead loss events or radiation damage (Fig. 4a–d). The weighted mean age of the Jiguanshan diorite of ca. 1780 Ma suggests that the diorite body formed in the late Paleoproterozoic.

4.2 Whole-rock geochemical composition

SiO_2 contents of the Jiguanshan diorite vary between 55.57 wt % and 59.44 wt % and the sum of $\text{K}_2\text{O} + \text{Na}_2\text{O}$ from 5.57 wt % to 6.03 wt %, corresponding to gabbroic diorite to diorite composition according to the TAS diagram (Fig. 5a). K_2O contents range from 2.97 wt % to 3.21 wt % and fall within the high-K calc-alkaline fields (Fig. 5b). The samples from the Jiguanshan diorite have consistent A / CNK ratios ranging from 0.78 to 0.81 and $\text{A} / \text{NK} > 1$, which classify them as metaluminous rocks (Fig. 5c). $\text{Mg}^{\#}$

($\text{Mg}^{\#} = (\text{MgO} + \text{FeO}_{\text{total}}) / \text{MgO} \times 100$) values range from 34 to 39 (Fig. 5d).

The Jiguanshan diorite depicts enrichment in large ion lithophile elements (LILE), such as Rb, Ba, and K, and negative anomalies of Sr, Ti, Nb, and Ta (Fig. 6a). $\sum \text{REE}$ contents range from 361 to 393 ppm. Light rare earth elements (LREE) exhibit stronger enrichment, while heavy rare earth elements (HREE) are relatively depleted (Fig. 6b). $(\text{La} / \text{Yb})_{\text{N}}$ ratios range from 12.2 to 15.0 (subscript N denotes normalization against chondrite La and Yb contents) with Eu / Eu^* ($\text{Eu} / \text{Eu}^* = 2\text{Eu}_{\text{N}} / (\text{Sm}_{\text{N}} + \text{Gd}_{\text{N}})$, subscript N denotes normalization against chondrite Sm and Gd contents) ratios ranging from 0.57 to 0.68 (Table 1).

4.3 Whole-rock Sr-Nd-Pb isotope compositions

All initial radiogenic isotope values and the errors of the initial Sr, Nd and Pb isotope ratios reported herein are calculated back to an age of 1780 Ma. The measured $^{87}\text{Sr} / ^{86}\text{Sr}$ ratios for the Jiguanshan diorites vary from 0.715177 ± 0.000011 to 0.724714 ± 0.000012 (2σ). Initial Sr ratios range from 0.7020 ± 0.0007 to 0.7058 ± 0.0010 (2σ , Fig. 7a). Measured $^{143}\text{Nd} / ^{144}\text{Nd}$ values vary from 0.511129 ± 0.000008 to 0.511329 ± 0.000007 (2σ). Initial $^{143}\text{Nd} / ^{144}\text{Nd}$ isotope compositions range from 0.509924 ± 0.000061 to 0.510090 ± 0.000063 (2σ), corresponding to initial ε_{Nd} values of -8.04 ± 1.20 to -4.80 ± 1.23 (2σ , Fig. 7b) and two-stage Nd model ages (T_{DM2}) of 2.94 to 2.68 Ga. Pb isotopic com-

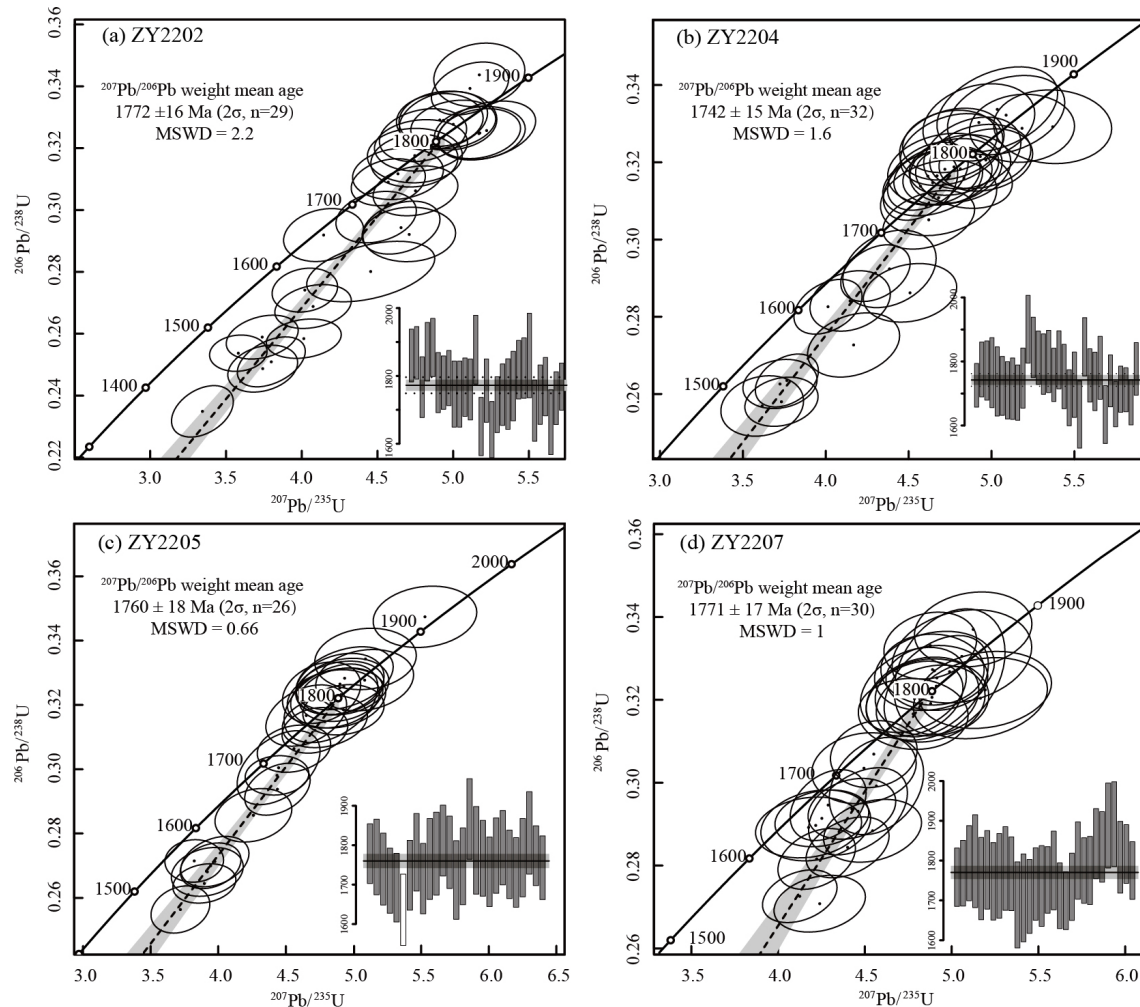


Figure 4. (a-d) Zircon U-Pb Concordia diagrams for the Jiguanshan diorite.

positions are as follows: $^{206}\text{Pb} / ^{204}\text{Pb} = 15.832\text{--}16.167$, $^{207}\text{Pb} / ^{204}\text{Pb} = 15.170\text{--}15.243$, and $^{208}\text{Pb} / ^{204}\text{Pb} = 36.046\text{--}37.324$. Initial Pb isotope ratios are significantly lower: $^{206}\text{Pb} / ^{204}\text{Pb}_i$ ratios ranging from 14.965 to 15.295, $^{207}\text{Pb} / ^{204}\text{Pb}_i$ ratios ranging from 15.090 to 15.150, $^{208}\text{Pb} / ^{204}\text{Pb}_i$ ratios ranging from 34.398 to 35.825, with $^{238}\text{U} / ^{204}\text{Pb}$ and $^{232}\text{Th} / ^{238}\text{U}$ ratios ranging from 2.3 to 2.9 and 5.3 to 7.8, respectively (Fig. 8).

5 Discussion

5.1 Composition of late-Paleoproterozoic diorites of the NCC

On a regional scale, the late Paleoproterozoic diorites of the NCC are distributed in a roughly east to west direction, unlike the north-northwest (NNW) strike, that characterizes the contemporaneous mafic dykes (Hou et al., 2008; Peng et al., 2007, 2008). Intrusion ages of the diorites are concentrated

between 1780 and 1750 Ma. All diorites have similar geochemical and isotopic compositions and can be regarded as a compositional homogeneous rock group.

Most of the late-Paleoproterozoic diorites of the NCC have silica contents in the range of 52 wt %–62 wt % (Fig. 5a). Total alkali content ($\text{K}_2\text{O} + \text{Na}_2\text{O}$) of 5 wt %–7 wt % suggests a subalkaline character (Fig. 5a). K_2O contents range from 2 wt %–5 wt % in accordance with a high-K calc-alkaline to shoshonite composition (Fig. 5b). The ASI and $\text{Mg}^\#$ values of the samples, except for a few data points that deviate significantly, are mostly homogeneous, with weighted average values of 0.81 and 37, respectively (Fig. 5c, d). In primitive mantle normalization multi-element diagrams, all diorites display enrichment of LILEs, such as Rb, Ba, and K, and depletion of high field strength elements (HFSEs), such as Na, Ta, Th, U, and Ti (Fig. 6). On the rare earth element normalization diagrams, they display negative Eu anomalies with enrichment in LREEs and a flat pattern of HREEs (Fig. 6).

Table 2. Whole-rock Sr isotopic compositions of the late Paleoproterozoic diorites in the NCC.

Sample	Age (Ma)	Rb (ppm)	Sr (ppm)	Rb / Sr	$^{87}\text{Rb} / ^{86}\text{Sr}$	$^{87}\text{Sr} / ^{86}\text{Sr}$	$\pm 2 \text{ SE}$	$^{87}\text{Sr} / ^{86}\text{Sr}$ (<i>t</i>)	Error (abs.)	Data source
Jiguanshan diorite										
ZY2201	1780	80.3	412	0.20	0.5648	0.71931	0.000010	0.70485	0.00077	
ZY2202	1780	95.2	374	0.25	0.7371	0.72471	0.000012	0.70584	0.00099	
ZY2203	1780	97.8	384	0.25	0.7377	0.72434	0.000011	0.70546	0.00099	
ZY2204	1780	88.4	406	0.22	0.6307	0.72111	0.000011	0.70496	0.00085	This study
ZY2205	1780	88.0	403	0.22	0.6334	0.71856	0.000011	0.70235	0.00086	
ZY2206	1780	89.5	542	0.17	0.4780	0.71518	0.000011	0.70294	0.00066	
ZY2207	1780	88.9	490	0.18	0.5252	0.71542	0.000013	0.70198	0.00072	
Wafang diorite										
WF1307-3	1780	107.0	389	0.28	0.7969	0.72131	0.000013	0.70091	0.00106	
WF1307-4	1780	109.0	400	0.27	0.7895	0.72144	0.000014	0.70123	0.00105	
WF1307-5	1780	84.0	411	0.20	0.5921	0.72024	0.000016	0.70508	0.00080	Wang et al. (2016)
WF1307-8	1780	113.0	343	0.33	0.9548	0.72479	0.000016	0.70035	0.00127	
WF1307-9	1780	110.0	373	0.29	0.8545	0.72236	0.000014	0.70048	0.00114	
Shizhaigou diorite										
Ln-1	1780	103.7	272	0.38	1.1040	0.72874	0.000012	0.70048	0.00146	
Ln-2	1780	101.5	322	0.31	0.9125	0.72868	0.000015	0.70532	0.00121	
Ln-3	1780	136.4	200	0.68	1.9758	0.72509	0.00001	0.67452	0.00259	Cui et al. (2011)
Ln-4	1780	116.6	295	0.40	1.1479	0.73149	0.000015	0.70210	0.00152	
Ln-5	1780	112.5	300	0.38	1.0885	0.72997	0.000014	0.70211	0.00144	
E-W Group dyke										
02SX001	1780	154.8	470	0.33	0.9542	0.72970	0.000014	0.70528	0.00127	
02SX007	1780	81.2	450	0.18	0.5231	0.71858	0.000014	0.70519	0.00072	
03LF01	1780	74.4	449	0.17	0.4801	0.71619	0.000013	0.70390	0.00066	Peng et al. (2007)
03FS04	1780	131.8	229	0.58	1.6748	0.74399	0.000012	0.70112	0.00220	
03FS07	1780	106.0	539	0.20	0.5699	0.71852	0.000013	0.70393	0.00078	
Weight mean value								0.70519	0.00031	(<i>n</i> = 8, calculated by IsoplotR)

$$(^{87}\text{Sr} / ^{86}\text{Sr})_s = (^{87}\text{Sr} / ^{86}\text{Sr})_0 + (^{87}\text{Rb} / ^{86}\text{Sr})_s \times (e^{\lambda t} - 1)$$

$$\lambda_{^{87}\text{Rb}} = 1.42 \times 10^{-11} \text{ a}^{-1}$$

Error of initial ratio is calculated from the measurement error of the isotope ratio, the estimated concentration error and the age error. The decay constant is considered to be a fixed value.

$$\sigma_{\text{Sr}(t)} = \sqrt{\sigma_{\text{Sr}}^2 + \sigma_{\text{Rb}}^2 (e^{\lambda t} - 1)^2 + \sigma_t^2 \left(\lambda e^{\lambda t} \left(\frac{\sigma_{\text{Rb}}}{\sigma_{\text{Sr}}} \right)^2 \right)}$$

$\sigma_{\text{Sr}(t)}$ is mean-square deviation of $(^{87}\text{Sr} / ^{86}\text{Sr})_t$

σ_{Rb} is mean-square deviation of $(^{87}\text{Rb} / ^{86}\text{Sr})_s$

σ_t is mean-square deviation of age.

All diorites have similar Nd isotopic compositions with a mean initial ϵ_{Nd} value of -6.5 ± 0.2 (2σ , $n = 41$, Fig. 7b). The overall range of initial ϵ_{Nd} values is from -10.2 ± 1.2 to -4.8 ± 1.2 (2σ , Fig. 7b). Some samples from the Wafang diorite (or Muzhijie diorite, Ma et al., 2023b; Wang et al., 2016) have enriched Nd isotope composition, which can be explained by assimilation or contamination of continental crust due to their higher zirconium content (Fig. 7b; Table 3). Overall, the initial ϵ_{Nd} values and the corresponding two-stage Nd model ages (T_{DM2}) of the diorites are consistent with each other except for the Wafang diorite (Table 3).

Initial ϵ_{Hf} values of zircons from the diorites in the NCC show a wide but consistent range of variations, i.e., from -17 to -2.5 in the Gushicun diorite (Ma et al., 2023a; Fig. 7c), from -14 to 0.55 in the Muzhijie diorite (Ma et al., 2023b; Fig. 7c), and from -17 to 0.95 in the Fudian diorite (Ma et al., 2023b; Fig. 7c).

al., 2023b; Fig. 7c). The diorites have similar Nd-Hf isotopic compositions and form a coherent group in geochemical diagrams, indicating a close relationship.

5.2 Initial Sr isotope composition and magma source characteristics

The late Paleoproterozoic diorites of the NCC show a large range in whole-rock initial Sr isotope composition (Fig. 7a). Determining magma sources for rocks with widely varying initial Sr ratios is complex, as Sr isotopes can be affected by magma mixing, assimilation, contamination, and melting degrees (e.g., Gao et al., 2015; Wolf et al., 2019; Zeng et al., 2005).

The whole-rock Nd and Sr isotope compositions of the diorites suggest a heterogeneous magma source (Fig. 7d). It might be argued that this could be the effect of mixing be-

Table 3. Whole-rock Nd isotopic compositions of the late Paleoproterozoic diorites in the NCC.

Sample	Age (Ma)	Nd (ppm)	Sm (ppm)	$^{147}\text{Sm} / ^{144}\text{Nd}$	$^{143}\text{Nd} / ^{144}\text{Nd}$	Error (2 s)	$^{143}\text{Nd} / ^{144}\text{Nd}$ (t)	Error (abs.)	$\varepsilon_{\text{Nd}}(t)$	Error (ε_{Nd})	T_{DM2} (Ga)	Data source
Jiguanshan diorite												
ZY2201	1780	72.3	12.7	0.1063	0.511238	0.000007	0.509994	0.000063	-6.69	1.24	2.83	
ZY2202	1780	71.2	12.1	0.1029	0.511129	0.000008	0.509924	0.000061	-8.04	1.20	2.94	
ZY2203	1780	70.9	12.0	0.1022	0.511131	0.000005	0.509934	0.000060	-7.85	1.19	2.93	
ZY2204	1780	73.2	12.7	0.1049	0.511240	0.000007	0.510011	0.000062	-6.35	1.22	2.80	This study
ZY2205	1780	80.0	14.0	0.1058	0.511329	0.000007	0.510090	0.000063	-4.80	1.23	2.68	
ZY2206	1780	72.9	12.8	0.1058	0.511317	0.000005	0.510078	0.000063	-5.03	1.23	2.70	
ZY2207	1780	77.1	13.4	0.1054	0.511320	0.000006	0.510086	0.000062	-4.88	1.22	2.68	
E-W Group dyke												
02SX001	1780	113	20.3	0.1084	0.511287	0.000009	0.510018	0.000065	-6.21	1.27	2.79	
02SX007	1780	62.6	11.3	0.1093	0.511285	0.000010	0.510005	0.000065	-6.47	1.28	2.81	
03LF01	1780	45.1	8.36	0.1120	0.511358	0.000017	0.510047	0.000068	-5.64	1.34	2.75	Peng et al. (2007)
03FS04	1780	102	17.5	0.1039	0.511270	0.000010	0.510053	0.000062	-5.53	1.22	2.74	
03FS07	1780	62.7	11.1	0.1068	0.511297	0.000013	0.510047	0.000064	-5.65	1.26	2.75	
Shizhaigou diorite												
Ln-1	1780	69.0	12.3	0.1075	0.511280	0.000012	0.510021	0.000065	-6.15	1.26	2.79	
Ln-2	1780	66.4	11.7	0.1065	0.511270	0.000011	0.510023	0.000064	-6.10	1.25	2.78	
Ln-3	1780	61.9	11.2	0.1090	0.511280	0.000011	0.510003	0.000065	-6.50	1.28	2.82	Cui et al. (2011)
Ln-4	1780	71.1	12.6	0.1072	0.511260	0.000011	0.510005	0.000064	-6.46	1.26	2.81	
Ln-5	1780	69.4	12.3	0.1072	0.511260	0.000012	0.510005	0.000064	-6.46	1.26	2.81	
Wafang diorite												
WF1307-3	1780	78.4	13.7	0.1056	0.511169	0.000008	0.509953	0.000062	-7.90	1.23	2.93	
WF1307-4	1780	78.5	14.1	0.1086	0.511215	0.000008	0.509965	0.000063	-7.67	1.26	2.91	
WF1307-5	1780	75.9	13.7	0.1091	0.511192	0.000008	0.509936	0.000064	-8.24	1.27	2.96	Wang et al. (2016)
WF1307-8	1780	77.6	13.4	0.1044	0.511039	0.000007	0.509837	0.000061	-10.2	1.21	3.11	
WF1307-9	1780	77.5	13.9	0.1084	0.511193	0.000005	0.509945	0.000063	-8.07	1.26	2.94	
Gushicun diorite												
20XRδ-1	1780	58.0	10.9	0.1134	0.511327	0.000004	0.509999	0.000067	-6.58	1.31	2.82	
20XRδ-3	1780	63.3	11.7	0.1118	0.511334	0.000006	0.510025	0.000066	-6.08	1.30	2.78	Ma et al. (2023a)
20XRδ-4	1780	59.1	10.9	0.1118	0.511341	0.000006	0.510032	0.000066	-5.94	1.30	2.77	
20XRδ-5	1780	53.1	9.9	0.1122	0.511354	0.000006	0.510041	0.000066	-5.77	1.30	2.76	
The Muzhijie diorites												
208Pt2-1	1780	63.5	11.5	0.1090	0.511297	0.000004	0.510021	0.000064	-6.15	1.26	2.79	
208Pt2-3	1780	64.2	11.7	0.1100	0.511300	0.000004	0.510012	0.000065	-6.33	1.27	2.80	
208Pt2-5	1780	66.4	12.3	0.1122	0.511295	0.000007	0.509982	0.000067	-6.92	1.30	2.85	
208Pt2-7	1780	72.1	13.1	0.1101	0.511297	0.000008	0.510007	0.000065	-6.42	1.28	2.81	Ma et al. (2023b)
208Pt2-9	1780	54.2	9.6	0.1076	0.511181	0.000006	0.509922	0.000064	-8.09	1.25	2.95	
208Pt2-11	1780	64.5	11.4	0.1073	0.511199	0.000006	0.509943	0.000064	-7.69	1.25	2.91	
208Pt2-13	1780	62.9	11.2	0.1076	0.511196	0.000008	0.509937	0.000064	-7.80	1.25	2.92	
208Pt2-16	1780	67.9	12.3	0.1098	0.511270	0.000007	0.509984	0.000065	-6.87	1.28	2.85	
Fudian diorite												
20XRSC-1	1780	65.8	12.1	0.1110	0.511309	0.000006	0.510009	0.000066	-6.39	1.29	2.81	
20XRSC-2	1780	67.1	12.3	0.1111	0.511315	0.000006	0.510014	0.000066	-6.30	1.29	2.80	
20XRSC-3	1780	69.5	12.8	0.1113	0.511314	0.000004	0.510011	0.000066	-6.35	1.29	2.80	
20XRSC-4	1780	67.5	12.5	0.1117	0.511311	0.000007	0.510002	0.000066	-6.52	1.30	2.82	Ma et al. (2023b)
20XRSC-5	1780	70.1	12.9	0.1111	0.511311	0.000006	0.510010	0.000066	-6.37	1.29	2.81	
20XRSC-6	1780	68.9	12.7	0.1112	0.511324	0.000005	0.510022	0.000066	-6.14	1.29	2.79	
20XRSC-8	1780	71.7	12.9	0.1089	0.511331	0.000006	0.510056	0.000065	-5.46	1.26	2.75	
20XRSC-9	1780	76.6	13.9	0.1096	0.511325	0.000005	0.510042	0.000065	-5.74	1.27	2.75	
Weight mean value										-6.51	0.20	(n = 41, calculated by IsoplotR)

$$(^{143}\text{Nd} / ^{144}\text{Nd})_s = (^{143}\text{Nd} / ^{144}\text{Nd})_0 + (^{147}\text{Sm} / ^{144}\text{Nd})_s \times (e^{\lambda t} - 1)$$

$$\varepsilon_{\text{Nd}}(t) = [(^{143}\text{Nd} / ^{144}\text{Nd})_s / (^{143}\text{Nd} / ^{144}\text{Nd})_{\text{CHUR}(t)} - 1] \times 10000$$

$$T_{\text{DM2}} = 1/\lambda \times \ln [1 + [(^{143}\text{Nd} / ^{144}\text{Nd})_{\text{DM}} - (^{143}\text{Nd} / ^{144}\text{Nd})_s + (^{147}\text{Sm} / ^{144}\text{Nd})_s - (^{147}\text{Sm} / ^{144}\text{Nd})_{\text{CC}}] \times (e^{\lambda t} - 1)] / [(^{147}\text{Sm} / ^{144}\text{Nd})_{\text{DM}} - (^{147}\text{Sm} / ^{144}\text{Nd})_{\text{CC}}]$$

$$\lambda_{^{147}\text{Sm}} = 0.654 \times 10^{-11} \text{ a}^{-1}$$

$$(^{143}\text{Nd} / ^{144}\text{Nd})_{\text{DM}} = 0.51315$$

$$(^{147}\text{Sm} / ^{144}\text{Nd})_{\text{DM}} = 0.2137$$

$$(^{147}\text{Sm} / ^{144}\text{Nd})_{\text{CC}} = 0.12$$

Error of initial ratio is calculated from the measurement error of the isotope ratio, the estimated concentration error and the age error. The decay constant is considered to be a fixed value.

$$\sigma_{\text{Nd}}(t) = \sqrt{\sigma_{\text{Nd}}^2 + \sigma_{\text{Sm}}^2 (e^{\lambda t} - 1)^2 + \sigma_t^2 (\lambda e^{\lambda t} \left(\frac{^{147}\text{Sm}}{^{144}\text{Nd}} \right)^2)}$$

$$\sigma_{\text{Nd}}(t)$$
 is mean-square deviation of $(^{143}\text{Nd} / ^{144}\text{Nd})_t$

$$\sigma_{\text{Sm}}(t)$$
 is mean-square deviation of $(^{143}\text{Sm} / ^{144}\text{Nd})_s$

$$\sigma_t$$
 is mean-square deviation of age

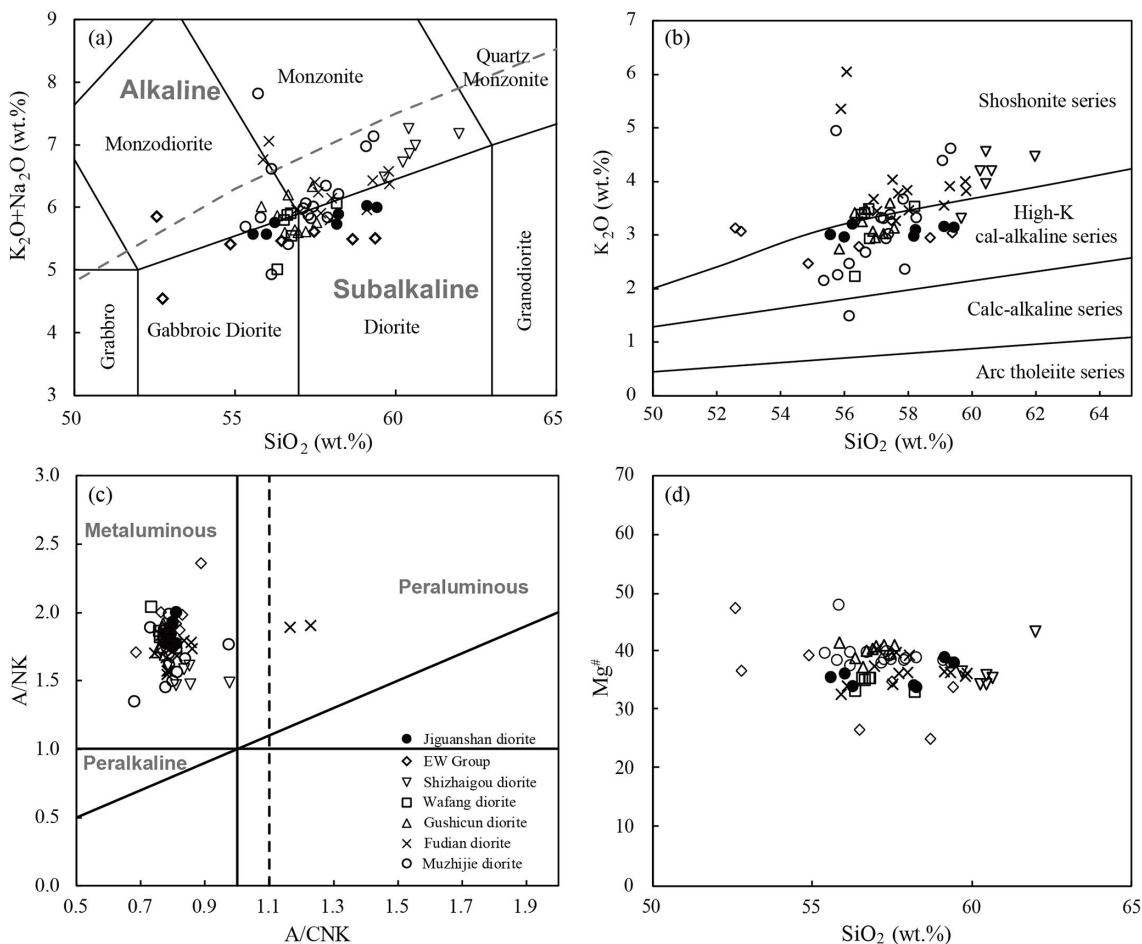


Figure 5. Plots of major elements for the diorites: (a) TAS diagram (after Le Bas et al., 1986); (b) K_2O content (wt %) versus SiO_2 content (wt %) (after Peccerillo and Taylor, 1976); (c) A/NK versus A/CNK values (after Maniar and Piccoli, 1989) (d) $Mg^{\#}$ value versus SiO_2 content (wt %).

tween crustal and mantle sources. However, mantle-derived rocks often have high MgO contents and elevated compatible element concentrations such as Ni and Cr, which is inconsistent with the element characteristics of the diorites (Table 1, see previous references). Variability in Sr isotope ratios can result from different degrees of source melting. However, a mica- or feldspar-rich source with high Rb/Sr ratios can produce melts with more radiogenic $^{87}Sr/^{86}Sr$ ratios (e.g., Hu et al., 2018). Melts affected by dehydration of amphibole typically have low $^{87}Sr/^{86}Sr$ ratios and adakitic characteristics (e.g., Rapp and Watson, 1995; Wolf and Wyllie, 1993). Thus, different degrees of source melting are unlikely to be the main cause for the isotopic composition of the diorites.

Initial $^{87}Sr/^{86}Sr$ ratios < 0.704 are negatively correlated with the $^{87}Rb/^{86}Sr$ ratios (Fig. 7a). For initial $^{87}Sr/^{86}Sr$ ratios > 0.704 , such correlation does no longer exist. A reason for this could be the large uncertainty propagation of the initial whole-rock Sr isotope ratios especially for old samples. Among all diorites there are samples with initial $^{87}Sr/^{86}Sr$ ratios > 0.704 . Excluding outliers, the mean average initial

$^{87}Sr/^{86}Sr$ ratio is 0.7052 ± 0.0003 ($2\sigma, n = 8$), which might represent the initial Sr isotope composition of the magma source (Fig. 7a).

The initial Sr ratios of the Xiong'er Group rocks vary widely and tend to be more radiogenic compared to the diorites (Fig. 7d). The initial Sr ratios of the diorites are more similar to lower crustal Archean xenoliths from the southeastern NCC (initial $^{87}Sr/^{86}Sr$ ratios: 0.7039–0.7068, $t = 1780$ Ma, e.g., Huang et al., 2004), suggesting that they are more likely associated with lower crustal rocks of the NCC rather than an enriched mantle source like the volcanic rocks of the Xiong'er Group.

5.3 Petrogenesis of the dioritic rocks

Several models have been proposed for the petrogenesis of intermediate dioritic rocks including partial melting of metasomatized mantle (e.g., Chen et al., 2021), partial melting of subducted oceanic crust and subsequent melt-peridotite reaction (e.g., Kelemen, 1995; Stern and Kilian, 1996), magma

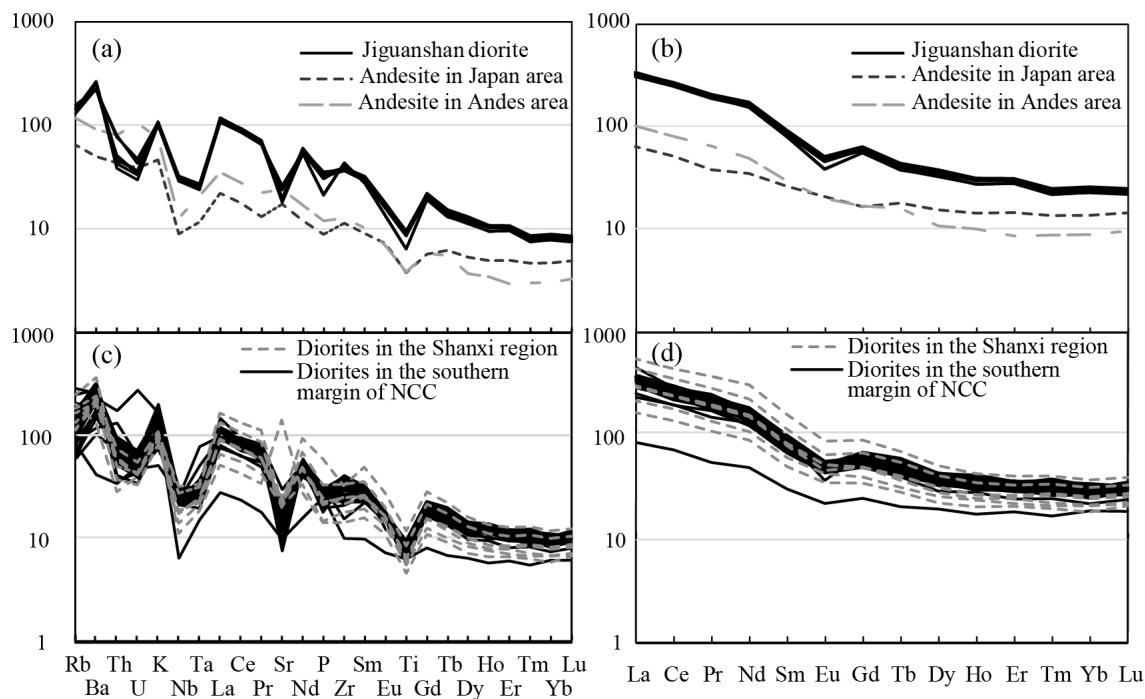


Figure 6. Primitive-mantle normalized trace element spider diagrams and chondrite-normalized REE patterns for the diorites. Normalization values from Sun and McDonough (1989); Diorites in Shanxi region from Peng et al. (2007), diorites in the southern margin of the NCC from Cui et al. (2011), Ma et al. (2023a, b), Wang et al. (2016), and Zhao et al. (2004). Average trace element compositions of intermediate rocks in the Japan and Andes arc are from Pan et al. (2017).

mixing/mingling (e.g., Reubi and Blundy, 2009; Streck et al., 2007), melting of basaltic rocks (e.g., Jackson et al., 2003; Petford and Atherton, 1996), as well as fractional crystallization of basaltic magmas (e.g., Castillo et al., 1999).

The diorites from the NCC have low compatible element concentrations, suggesting that they were not derived directly from a mantle source (Fig. 9a). Larger contribution of mantle material can also be excluded due to their initial Nd isotope features (Fig. 7b), silica and $Mg^{\#}$ values (Fig. 5d).

Partial melting of subducting oceanic crust can also form rocks of intermediate composition, such as adakites, which often exhibit high Sr / Y ratios (> 20) and low Y contents (< 18 ppm) (e.g., Defant and Drummond, 1990; Peacock et al., 1994). The Jiguanshan and other diorites from the NCC have relatively high Y and Sr contents with Sr / Y ratios < 15 . Thus, partial melting of oceanic crust does not appear to have played a role during the genesis of the diorites.

Cr contents decrease with decreasing MgO, indicating fractionation of clinopyroxene (Fig. 9a). CaO contents decrease with increasing SiO₂, suggesting crystallization of minerals, such as plagioclase or clinopyroxene (Fig. 9b). However, Al₂O₃ and Na₂O contents do not significantly decrease with increasing SiO₂, indicating that plagioclase and clinopyroxene were not significant fractionation phases (Fig. 9c–d). The increase in K₂O contents with increasing SiO₂ suggests no biotite and/or K-feldspar fractionation dur-

ing magmatic evolution (Fig. 9e). Increasing SiO₂ with decreasing TiO₂ indicate crystallization and fractionation of Ti-bearing minerals, such as ilmenite (Fig. 9f). Eu / Eu* values of the diorites do not show significant changes with Sr contents, which provides evidence that fractionation of plagioclase from the melt was not significant (Fig. 9g).

From the above discussion, it can be concluded that the petrogenesis of the diorites in the NCC was associated with minor fractional crystallization processes. Whole-rock La / Yb versus La and Zr / Sm versus Zr correlations are as expected for a partial melting process (Fig. 9h–i). This implies that the formation of the diorites may be closely related to the partial melting of a basaltic protolith.

Basement rocks of the lower Taihua Group at the southern margin of the NCC consist of amphibolite (e.g., Diwu et al., 2014, 2018; Wang et al., 2020). Partial melting of amphibolite can lead to the production of intermediate to acidic magmas (e.g., Beard and Lofgren, 1991; Rapp and Watson, 1995). The amphibolites of the Taihua Group are characterized by low K content and low K₂O / Na₂O ratios (< 0.5 , Wang et al., 2019), making it difficult to generate high-K₂O rocks (Beard and Lofgren, 1991; Roberts and Clemens, 1993). Partial melting of amphibolite typically results in the formation of peraluminous melts (e.g., Beard and Lofgren, 1991; Rapp and Watson, 1995), whereas the diorites in the NCC have low Al₂O₃ content and metaluminous character

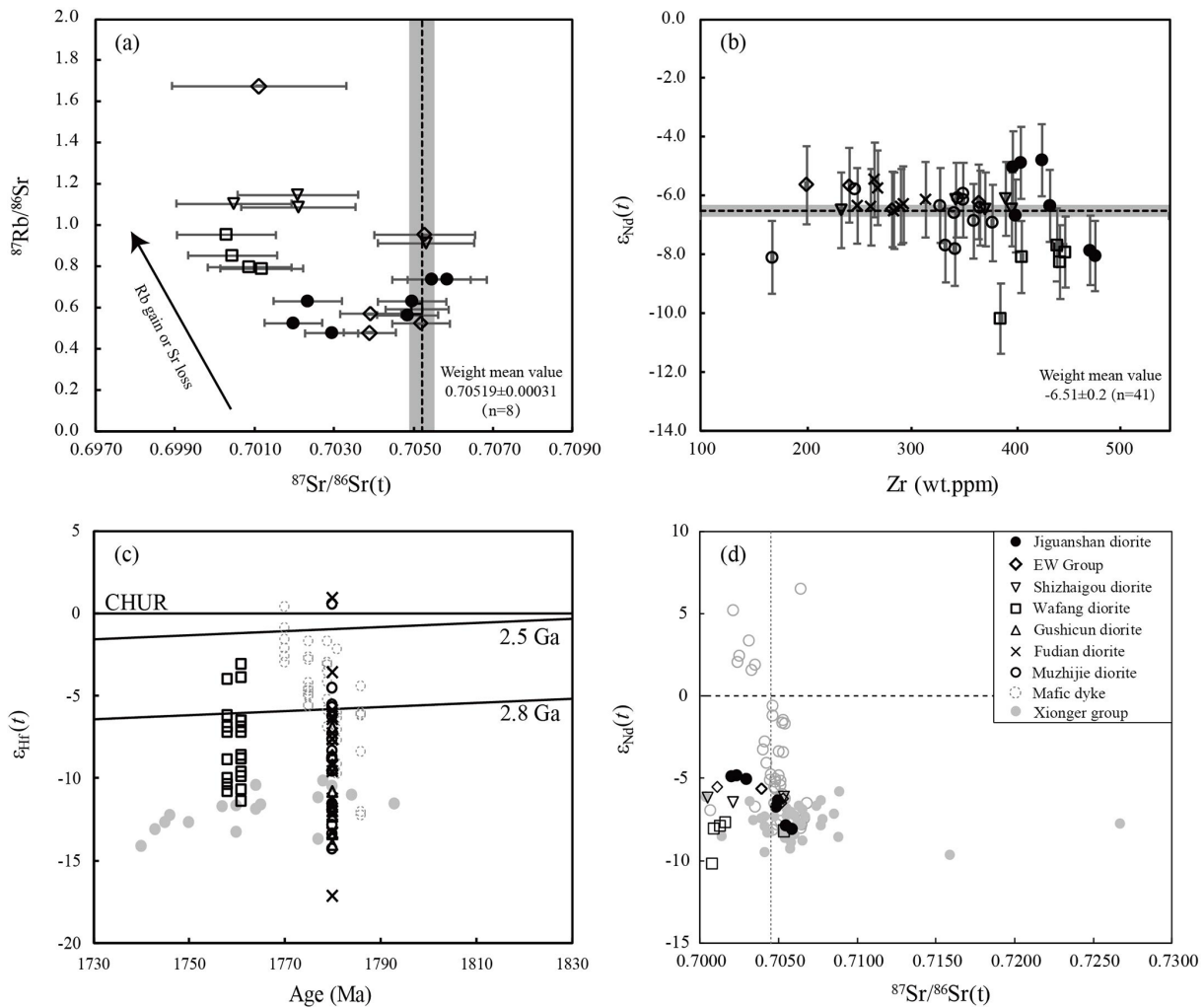


Figure 7. (a) $^{87}\text{Rb}/^{86}\text{Sr}$ versus $^{87}\text{Sr}/^{86}\text{Sr}(t)$ ratio; (b) $\varepsilon_{\text{Nd}}(t)$ value versus Zr content (ppm); (c) $\varepsilon_{\text{Hf}}(t)$ value versus age (Ma); (d) $\varepsilon_{\text{Nd}}(t)$ value versus $^{87}\text{Sr}/^{86}\text{Sr}(t)$ ratio. Data source for Xiong'er Group (Hf isotope composition from Wang et al., 2010; initial Sr isotope composition and initial ε_{Nd} value from He et al., 2008, 2010; Peng et al., 2008; Wang et al., 2010; Zhao et al., 2002); mafic dyke swarms (initial Sr isotope composition and initial ε_{Nd} value from Hu et al., 2010; Peng et al., 2007; Wang et al., 2004).

(Fig. 5c; Weighted average A / NCK values of 0.81). Additionally, the ε_{Nd} values of the Taihua Group amphibolites at $t = 1780$ Ma vary widely from -6.7 to 0.4 , different from those of the diorites (Wang et al., 2019). Therefore, it seems unlikely that the diorites formed by the partial melting of Taihua Group amphibolites.

Mafic rocks of the Xiong'er Group and mafic dyke swarms were argued to be the source of the diorites (Cui et al., 2011; Ma et al., 2023b; Peng et al., 2007). Such rocks possess a relatively large range of initial Sr and Nd isotopic compositions (Fig. 7d), while the initial Nd isotopic compositions of the diorites are relatively homogeneous (Fig. 7b). Whole-rock initial Nd ratios and zircon initial Hf isotope ratios of the Xiong'er Group rocks are also enriched (Fig. 7c). Initial Pb isotopic compositions of the mafic dykes and Xiong'er Group rocks are very radiogenic and variable (Fig. 8a, b),

which is due to the high U and Th contents of the protolith, indicating the presence of an enriched subcontinental lithospheric mantle source (e.g., Hou et al., 2008; Peng et al., 2004, 2007; Wang et al., 2004, 2010; Zhao et al., 2007). Based on the previous discussion, the geochemical characteristics of the diorites are more compatible with a crustal origin and the isotopic compositions of the diorites indicate that they were not derived from an enriched mantle source.

Additionally, the Xiong'er volcanic rocks have lower Nb / Ta ratios and Nb contents compared to the diorites (Fig. 10a). Nb and Ta share a similar valence state and atomic radii, but they can undergo fractionation during the subduction process (Jochum et al., 1986; Shannon, 1976). The Xiong'er volcanic rocks, with higher and positively correlated Ba / Th and Sr / Th ratios (Fig. 10a–b), likely originated from a source influenced by an early subduction com-

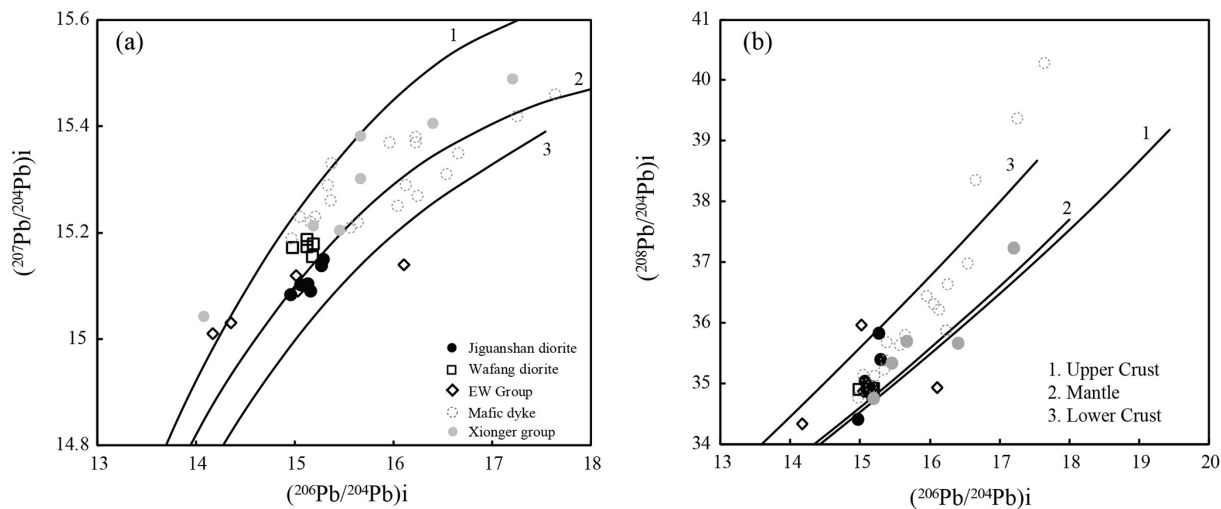


Figure 8. (a) $(^{207}\text{Pb} / ^{204}\text{Pb})_i$ versus $(^{206}\text{Pb} / ^{204}\text{Pb})_i$; (b) $(^{208}\text{Pb} / ^{204}\text{Pb})_i$ versus $(^{206}\text{Pb} / ^{204}\text{Pb})_i$. Data for Xiong'er Group from Zhao (2000), for mafic dyke swarms from Hu et al. (2010), Peng et al. (2007) and for diorites from Peng et al. (2007), Wang et al. (2016).

ponent, whereas the diorites appear to be less affected by early subduction-related materials. Therefore, it seems likely that the diorites were formed by partial melting of a mafic lower crustal protolith on top of an enriched subcontinental lithospheric mantle beneath the NCC.

5.4 Tectonic implications

After Paleoproterozoic collision and amalgamation, the NCC was intruded by diverse magmatic rocks, which have been interpreted as products of continental arc magmatism, post-collisional extension, or continental rift/mantle plume magmatism.

The volcanic rocks of the Xiong'er Group along the southern margin of the NCC are dominated by andesites, exhibiting calc-alkaline characteristics and negative Nb-Ta-Ti anomalies (Jia, 1985; He et al., 2009; Zhao et al., 2009). These signatures together with Nd isotope evidence for ancient crustal assimilation and multiphase volcanic activities, support a continental arc environment for the formation of the Xiong'er Group (He et al., 2009; Zhao et al., 2009).

The radially distributed mafic dike swarms, accompanied by A-type granite intrusions and rift-related sedimentary sequences, are indicative of a continental rift setting (e.g., Fan et al., 2024; Xu et al., 2008; Zhao et al., 2002, 2007). The Xiong'er Group is dominated by andesites, dacites, and rhyolites with minor basaltic andesites, which some researchers interpret as an atypical bimodal suite suggestive of a continental rift setting (Zhao et al., 2002, 2007). Furthermore, the 1.80 to 1.75 Ga old mafic dike swarms are distributed in a radial or concentric pattern centered on the Xiong'er Rift and extending northward (Peng et al., 2007). They share geochemical characteristics, such as high TiO_2 and MgO contents, enrichment in LREEs, Ba, and K, and depletion in Nb-

Ta which is interpreted as evidence for lithospheric extension induced by mantle plume upwelling (e.g., Hou et al., 2008; Peng et al., 2007, 2008).

The post-collisional extension model emphasizes that the late Paleoproterozoic magmatism occurred during lithospheric delamination and possibly slab detachment (e.g., Wang et al., 2004, 2008, 2014, 2023a). The mafic dikes are enriched in LILEs and LREEs but depleted in HFSEs, and show negative $\varepsilon_{\text{Nd}}(t)$ and $\varepsilon_{\text{Hf}}(t)$ values. This suggests derivation from an enriched lithospheric mantle previously metasomatized by subduction zone fluids (e.g., Hu et al., 2010; Wang et al., 2004, 2008, 2014). The dikes are concentrated in the Trans-North China Orogen and nearby areas, consistent with extensional fractures caused by a rising asthenosphere (Wang et al., 2004, 2008, 2014). Their geochemical features, lacking OIB or asthenospheric mantle affinities, do not support a mantle plume origin (Wang et al., 2014).

Calk-alkaline diorites are important intermediate rock that typically form at island arcs, subduction zones, and continental collision orogenic belts along convergent plate boundaries. Island arc intermediate rocks, such as boninites and andesites are generally characterized by high MgO , Cr, and Ni contents (Hickey and Frey, 1982; Rapp and Watson, 1995), whereas continental arc intermediate rocks typically show high Al_2O_3 content with a wider range of $^{87}\text{Sr} / ^{86}\text{Sr}$ and $^{143}\text{Nd} / ^{144}\text{Nd}$ isotope compositions, reflecting an obvious influence of continental crust or more enriched sources (Hawkesworth et al., 1979; Peacock et al., 1994). The Paleoproterozoic diorites of the NCC lack the compositional features of arc-related rocks, meanwhile, their trace element distributions differ from those of island arc and continental arc intermediate rocks. For example, the diorites do not show significant enrichment in Sr, Th, and U compared to arc-related rocks (Fig. 6a). The diorites also exhibit a negative

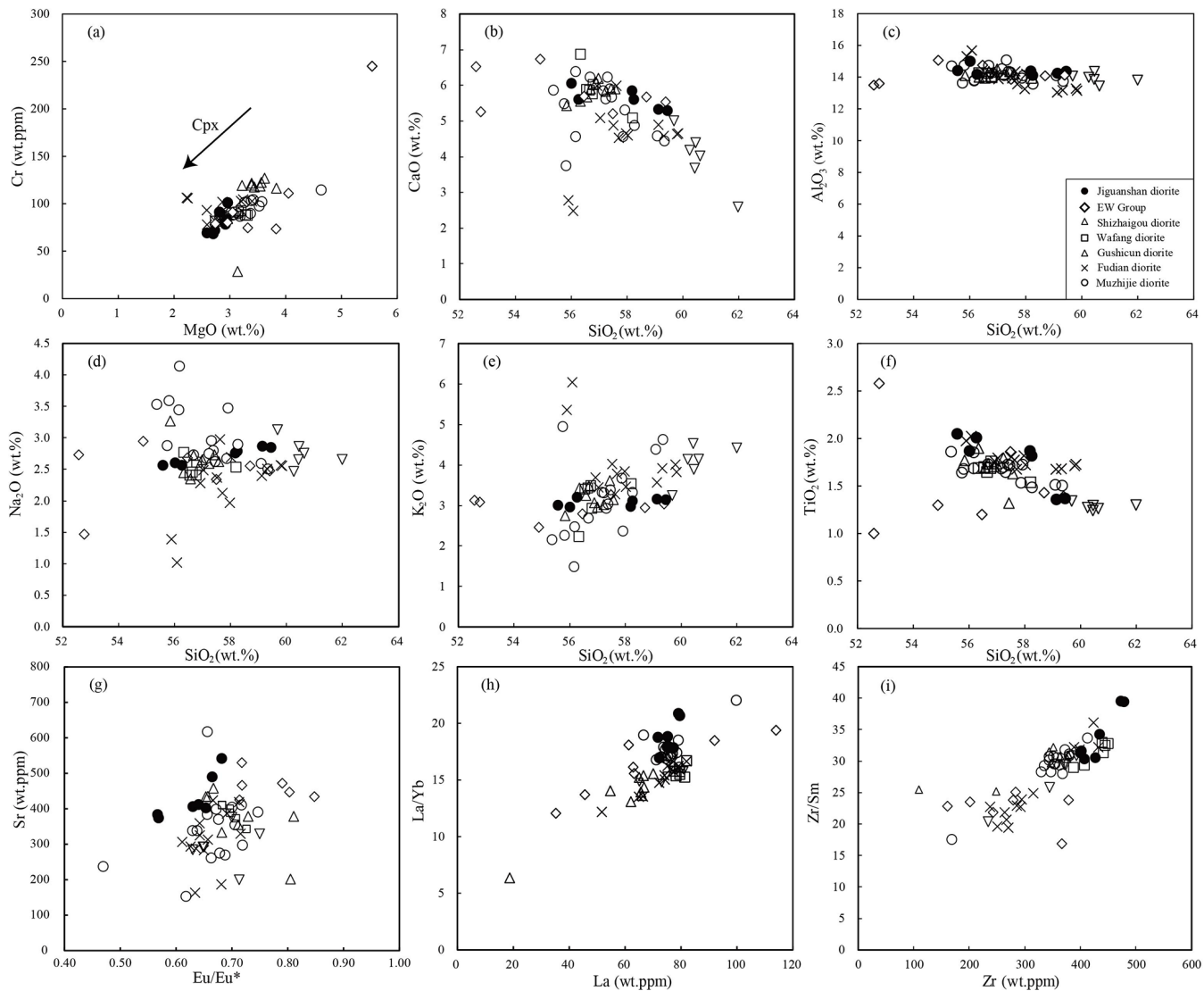


Figure 9. (a) Cr (ppm) content versus MgO content (wt %); (b) CaO (wt %) content versus SiO₂ content (wt %); (c) Al₂O₃ (wt %) content versus SiO₂ content (wt %); (d) Na₂O (wt %) content versus SiO₂ content (wt %); (e) K₂O (wt %) content versus SiO₂ content (wt %); (f) TiO₂ (wt %) content versus SiO₂ content (wt %); (g) Eu / Eu* value versus Sr content (ppm); (h) La / Yb value versus La content (ppm); (i) Zr / Sm value versus Zr content (ppm).

Eu anomaly in the REE diagram, which is different from arc-related rocks (Fig. 6b). Diorites in collisional orogenic belts have high MgO and K₂O contents and adakite-like characteristics with high Sr / Y and La / Yb ratios (Yang et al., 2015). However, Paleoproterozoic diorites of the NCC do not show typical arc-related element and isotopic signatures, suggesting formation in a non-subduction environment.

Diorites can also form during crustal extension (Asmerom et al., 1990; Liu et al., 2024). The NCC was in a post-collisional extensional setting after its final amalgamation (e.g., Zhai, 2010). During this stage, magmatism becomes more complex (Bonin, 2004). Zircon is a very stable mineral and its trace elements offer significant potential for distin-

guishing between different tectonic settings. For the following discussion, zircon samples with La contents (< 1 ppm) were selected to ensure accurate information from zircon trace element contents without interference from the inclusion of other accessory phases (Zou et al., 2019). All zircons from the diorites plot within the continental area in the U / Yb versus Y diagram (Fig. 11a), and most of them fall into a rift-controlled tectonic environment in tectonic discrimination diagrams (Fig. 11b, c; Carly et al., 2014).

Furthermore, HFSE elements, such as Zr, Nb, Ta, Hf, and Th, are important tectonic indices. The distinctive Th content in arc magmas is primarily due to its low solubility in subduction zone fluids and its contribution from sedi-

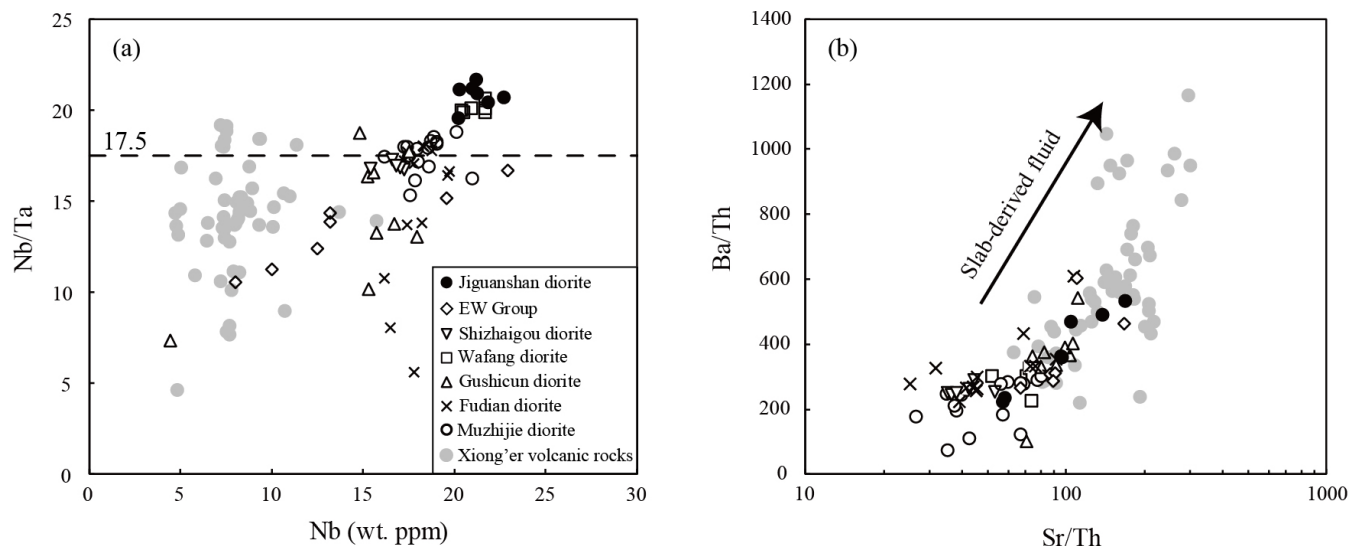


Figure 10. (a) Nb / Ta value versus Nb content (ppm); (b) Ba / Th value versus Sr / Th value; Data for Xiong'er Group from He et al. (2008, 2010), Wang et al. (2010), Zhao et al. (2002).

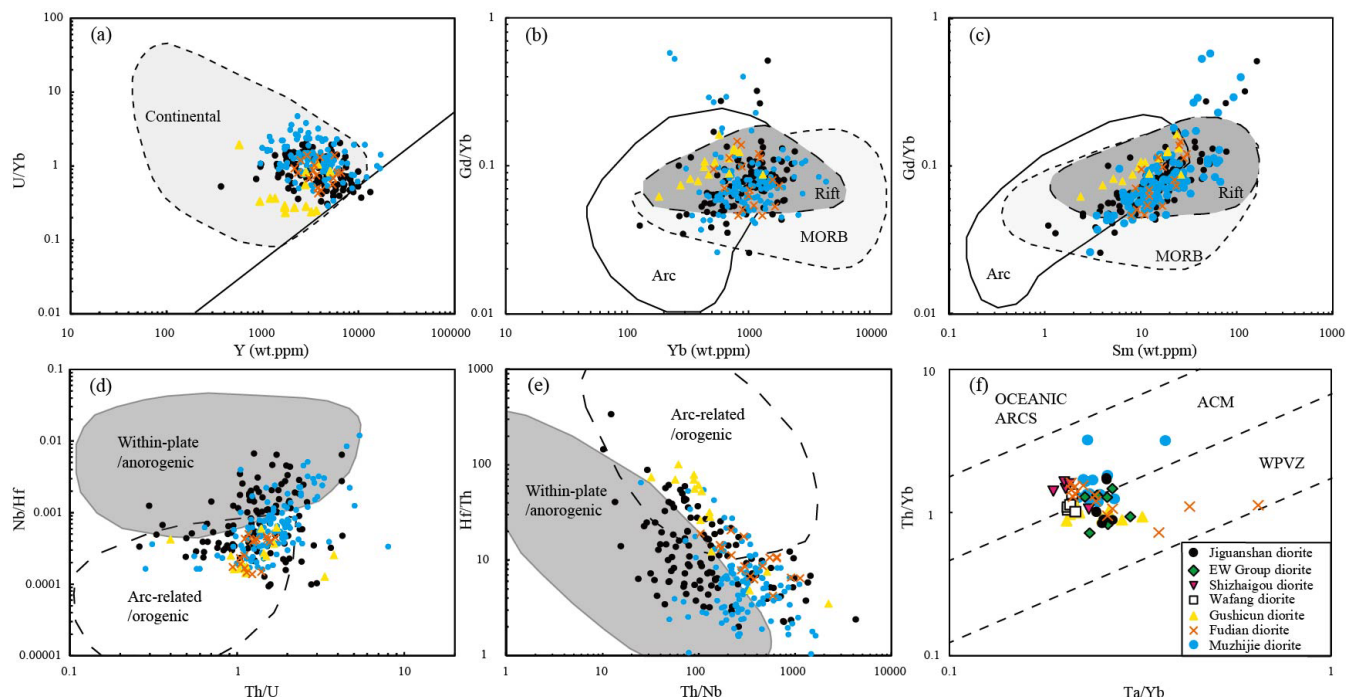


Figure 11. (a) Zircon trace element U / Yb ratio versus Y content (ppm) (after Grimes et al., 2007); (b) Zircon Gd / Yb ratio versus Yb content (ppm) (after Carley et al., 2014); (c) Zircon Gd / Yb ratio versus Sm content (ppm) (after Carley et al., 2014); (d) Zircon Nb / Hf ratio versus Th / U ratio (after Hawkesworth and Kemp, 2006); (e) Zircon Hf / Th ratio versus Th / Nb ratio (after Yang et al., 2012); (f) Whole-rock trace element Th / Yb ratio versus Ta / Yb ratio (after Pearce, 1983; Gorton and Schandl, 2000).

imentary components (e.g., Bailey and Ragnasdotir, 1994; Pearce and Peate, 1995). Arc-related/orogenic magmas usually have less Nb than those of within-plate settings (e.g., Pearce and Peate, 1995; Sun and McDonough, 1989). Nb in zircon is thought to be incorporated through xenotime-type

substitution (Schulz et al., 2006) and is suggested to reflect the magma composition with minimal influence of magmatic fractionation (Hoskin et al., 2000; Schulz et al., 2006). In the Nb / Hf versus Th / U and Hf / Th versus Th / Nb diagrams, zircons from the Fudian and Gushicun diorites plot

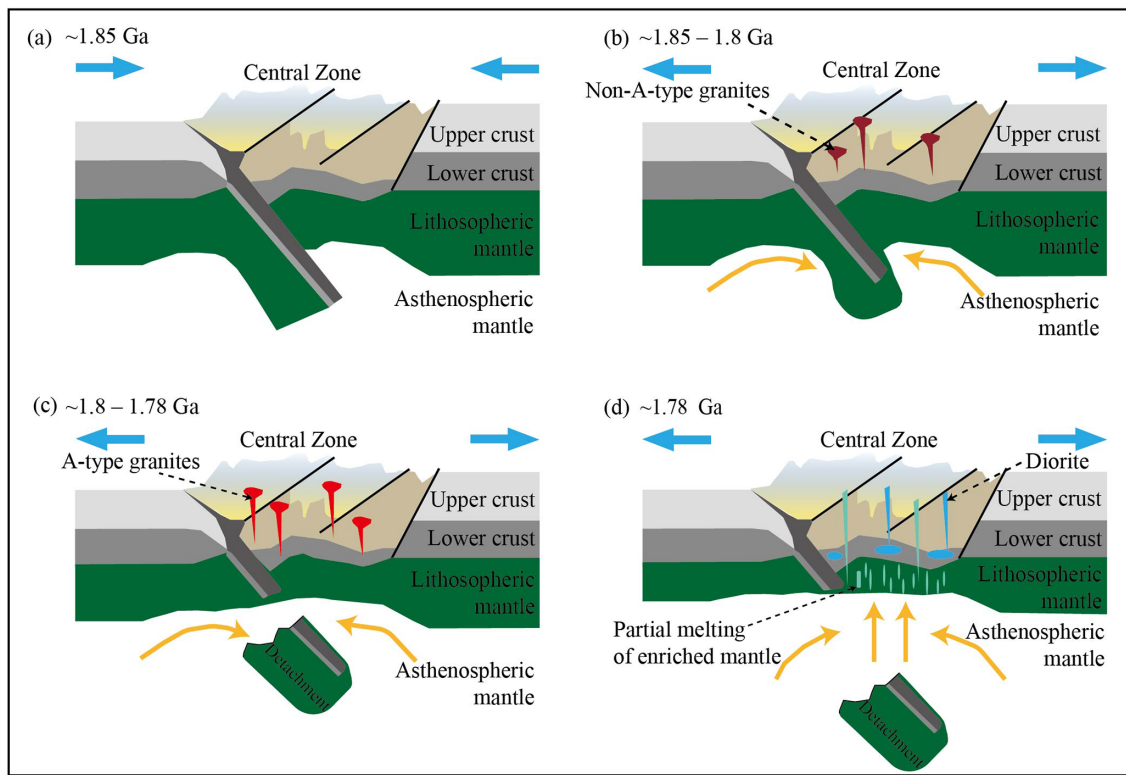


Figure 12. Tectonic evolution in the North China Craton during the Paleoproterozoic (after Wang et al., 2004; Deng et al., 2016a): (a) ~1.85 Ga: Western and Eastern Blocks collision; (b) ~1.85–1.8 Ga: Post-collisional crustal thickening and granite emplacement; (c) ~1.8–1.78 Ga: Post-collisional delamination and formation of A-type granite; (d) ~1.78 Ga: Transition from post-collisional to rift setting.

within or close to the arc-related/orogenic area (Fig. 11d, e). The Jiuganshan and Muzhijie diorites plot in the arc-related/orogenic and within-plate/anorogenic areas (Fig. 11d, e). Whole-rock Ta/Yb and Th/Yb ratios of the diorites are uniform (Fig. 11f), all falling within the overlapping area of the ACM (active continental margins) and WPVZ (within-plate volcanic zone). This may indicate that the post-collisional extension during this period proceeded continuously and progressively into a rift evolution. Thus, the diorites preserve a record of superposition of components from multiple tectonic settings.

After the ~1.85 Ga collisional event, the NCC entered into a prolonged post-collisional extensional stage (Fig. 12). During this stage, magmatism was primarily controlled by crustal thickening and remelting, leading to the widespread formation of various crust-derived granites (e.g., Geng et al., 2006; Zhao et al., 2008, 2018). Subsequent slab breakoff and gravitational collapse of the thickened crust triggered extension in the mid-upper crust and emplacement of felsic magmas (Deng et al., 2016a; Wang et al., 2023a; Xu et al., 2024). At ca. 1.78 Ga, lithospheric thinning induced upwelling of the asthenosphere, causing further partial melting of previously subduction-fluid-metasomatized lithospheric mantle (e.g., Peng et al., 2007, 2008; Wang et al., 2010, 2014; Zhao et al., 2002, 2007). Following this event, the magmatic ac-

tivity in this region became dominated by A-type granites and alkaline rocks, marking a transition to an anorogenic intracontinental extensional setting (e.g., Deng et al., 2016b; Wang et al., 2024). The 1.78 Ga old crust-derived diorites show transitional geochemical features, retaining some remnant effects of orogenic magmatism while gradually evolving toward intraplate magmatism. It reflects the ongoing extension of the NCC after its amalgamation.

6 Conclusions

The Jiguanshan diorite yields a U-Pb zircon age of ca. 1.78 Ga. The intrusion displays geochemical features in common with other Paleoproterozoic diorite intrusions of the NCC. The diorite emplaced contemporaneous with the Xiong'er volcanic rocks and the mafic dyke swarms, representing a significant period of magmatism in the NCC.

The diorites were produced by partial melting of a mafic protolith. The Sr-Nd-Pb-Hf isotopic characteristics indicate that the source was not the same as that for the Xiong'er volcanic rocks or the mafic dyke swarms. Instead, the diorites were likely derived from the lower crust of the NCC.

The formation of Paleoproterozoic diorites in the NCC was not connected with arc magmatism. Instead, it was asso-

Table 4. Whole-rock Pb isotopic compositions of the Jiguanshan diorite.

Spec.no	U (ppm)	Th (ppm)	Pb (ppm)	$^{206}\text{Pb} / ^{204}\text{Pb}$	$\pm 2\text{ SE}$	$^{207}\text{Pb} / ^{204}\text{Pb}$	$\pm 2\text{ SE}$	$^{208}\text{Pb} / ^{204}\text{Pb}$	$\pm 2\text{ SE}$	$^{206}\text{Pb} / ^{204}\text{Pb}$ initial	$^{207}\text{Pb} / ^{204}\text{Pb}$ initial	$^{208}\text{Pb} / ^{204}\text{Pb}$ initial	μ	$^{232}\text{Th} / ^{204}\text{Pb}$	$^{232}\text{Th} / ^{204}\text{Pb}$	ω
ZY2201	0.70	4.28	16.38	15.867	0.0005	15.189	0.0005	36.502	0.0014	15.063	15.103	35.027	2.6	16.0	16.0	6.3
ZY2202	0.98	6.43	21.20	16.167	0.0008	15.243	0.0009	37.126	0.0022	15.295	15.150	35.392	2.8	18.8	18.8	6.8
ZY2203	0.88	6.71	18.03	15.882	0.0006	15.182	0.0006	36.494	0.0013	14.965	15.084	34.398	2.9	22.8	22.8	7.8
ZY2204	0.71	4.27	16.29	16.097	0.0010	15.225	0.0009	37.324	0.0023	15.271	15.137	35.825	2.6	16.3	16.3	6.2
ZY2205	0.75	3.87	18.90	15.832	0.0007	15.179	0.0006	36.046	0.0016	15.095	15.100	34.901	2.3	12.4	12.4	5.3
ZY2206	0.61	3.22	15.22	15.914	0.0010	15.170	0.0010	36.124	0.0024	15.164	15.090	34.939	2.4	12.9	12.9	5.4
ZY2207	0.68	3.55	14.22	16.036	0.0008	15.199	0.0007	36.338	0.0016	15.136	15.103	34.931	2.9	15.3	15.3	5.4

Initial Pb isotopic ratios are calculated back to 1780 Ma.

ciated with a rift setting. The formation of diorite records the transition of crustal origin rocks from orogenic-related magmatism to intraplate magmatism during the post-collision extensional stage. It therefore reflects the ongoing extension of the NCC after its amalgamation.

Code availability. This study did not generate new custom code. All statistical analyses were performed using ICPMSDataCal software, Isoplot R and Microsoft Office. All figures were prepared using Adobe Illustrator and Microsoft Office.

Data availability. The data that support the findings of this study are available from the corresponding author upon reasonable request.

Supplement. The supplement related to this article is available online at <https://doi.org/10.5194/se-17-203-2026-supplement>.

Author contributions. ZW: Investigation, Writing – Review and Editing; JH and FC: Supervision, Writing – Review and Editing, Funding acquisition; WS: Conceptualization, Writing – Review and Editing; ST, YJ, JH: Data collection for this paper.

Competing interests. The contact author has declared that none of the authors has any competing interests.

Disclaimer. Publisher's note: Copernicus Publications remains neutral with regard to jurisdictional claims made in the text, published maps, institutional affiliations, or any other geographical representation in this paper. The authors bear the ultimate responsibility for providing appropriate place names. Views expressed in the text are those of the authors and do not necessarily reflect the views of the publisher.

Acknowledgements. We are deeply grateful to the anonymous reviewers for their valuable scientific and linguistic comments on the manuscript. We also thank P. Xiao and Z. H. Hou for their assistance during the analysis, and editor Yang Chu for his support.

Financial support. This research has been supported by the Strategic Priority Research Program of the Chinese Academy of Sciences (grant no. XDA0430203) and the National Natural Science Foundation of China (grant nos. 42202069 and 41872049). Zhiyi Wang was financially supported by China Scholarship Council (grant no. 202306340065).

Review statement. This paper was edited by Yang Chu and reviewed by two anonymous referees.

References

Asmerom, Y., Snow, J. K., Holm, D. K., Jacobsen, S. B., Wernicke, B. P., and Lux, D. R.: Rapid uplift and crustal growth in extensional environments: An isotopic study from the Death Valley region, California, *Geology*, 18, 223–226, [https://doi.org/10.1130/0091-7613\(1990\)018<0223:RUACGI>2.3.CO;2](https://doi.org/10.1130/0091-7613(1990)018<0223:RUACGI>2.3.CO;2), 1990.

Bailey, E. H. and Ragnarsdottir, K. V.: Uranium and thorium solubilities in subduction zone fluids, *Earth Planet. Sci. Lett.*, 124, 119–129, [https://doi.org/10.1016/0012-821X\(94\)00071-9](https://doi.org/10.1016/0012-821X(94)00071-9), 1994.

Beard, J. S. and Lofgren, G. E.: Dehydration melting and water-saturated melting of basaltic and andesitic greenstones and amphibolites at 1, 3, and 6.9 kb, *J. Petrol.*, 32, 365–401, <https://doi.org/10.1093/petrology/32.2.365>, 1991.

Bonin, B.: Do coeval mafic and felsic magmas in post-collisional to within-plate regimes necessarily imply two contrasting, mantle and crustal sources? A review, *Lithos*, 78, 1–24, <https://doi.org/10.1016/j.lithos.2004.04.042>, 2004.

Carley, T. L., Miller, C. F., Wooden, J. L., Padilla, A. J., Schmitt, A. K., Economos, R. C., Bindeman, I. N., and Jordan, B. T.: Iceland is not a magmatic analog for the Hadean: evidence from the zircon record, *Earth Planet. Sc. Lett.*, 405, 85–97, <https://doi.org/10.1016/j.epsl.2014.08.015>, 2014.

Castillo, P., Janney, P., and Solidum, R.: Petrology and geochemistry of Camiguin Island, southern Philippines: insights to the source of adakites and other lavas in a complex arc setting, *Contrib. Mineral. Petrol.*, 134, 33–51, <https://doi.org/10.1007/s004100050467f-1999>.

Chen, F., Hegner, E., and Todt, W.: Zircon ages, Nd isotopic and chemical compositions of orthogneisses from the Black Forest, Germany – evidence for a Cambrian magmatic arc, *Int. J. Earth Sci.*, 88, 791–802, <https://doi.org/10.1007/s005310050306>, 2000.

Chen, F., Li, X. H., Wang, X. L., Li, Q. L., and Siebel, W.: Zircon age and Nd-Hf isotopic composition of the Yunnan Tethyan belt, southwestern China, *Int. J. Earth Sci.*, 96, 1179–1194, <https://doi.org/10.1007/s00531-006-0146-y>, 2007.

Chen, L., Zheng, Y. F., Xu, Z., and Zhao, Z. F.: Generation of andesite through partial melting of basaltic metasomatites in the mantle wedge: Insight from quantitative study of Andean andesites, *Geosci. Front.*, 12, 101124, <https://doi.org/10.1016/j.gsf.2020.12.005>, 2021.

Cui, M. L., Zhang, B. L., Peng, P., Zhang, L. C., Shen, X. L., Guo, Z. H., and Huang, X. F.: Zircon/baddeleyite U-Pb dating for the Paleoproterozoic intermediate-acid intrusive rocks in Xiaoshan Mountains, west of Henan Province and their constraints on the age of the Xiong'er Volcanic Province, *Acta Petrol. Sin.*, 26, 1541–1549, 2010 (in Chinese with English abstract).

Cui, M. L., Zhang, B. L., and Zhang, L. C.: U-Pb dating of baddeleyite and zircon from the Shizhaigou diorite in the southern margin of North China Craton: Constraints on the timing and tectonic setting of the Paleoproterozoic Xiong'er group, *Gondwana Res.*, 20, 184–193, <https://doi.org/10.1016/j.gr.2011.01.010>, 2011.

Defant, M. and Drummond, M.: Derivation of some modern arc magmas by melting of young subducted lithosphere, *Nature*, 347, 662–665, <https://doi.org/10.1038/347662a0>, 1990.

Deng, X. Q., Peng, T. P., and Zhao, T. P.: Geochronology and Geochemistry of the Late Paleoproterozoic Aluminous A-Type Granite in the Xiaoqinling Area along the Southern Margin of the North China Craton: Petrogenesis and Tectonic Implications, *Precambrian Res.*, 285, 127–146, <https://doi.org/10.1016/j.precamres.2016.09.013>, 2016a

Deng, X. Q., Zhao, T. P., and Peng, T. P.: Age and geochemistry of the early Mesoproterozoic A-type granites in the southern margin of the North China Craton: Constraints on their petrogenesis and tectonic implications, *Precambrian Research*, 283, 68–88, <https://doi.org/10.1016/j.precamres.2016.07.018>, 2016b.

Diwu, C. R., Sun, Y., Zhao, Y., and Lai, S. C.: Early Paleoproterozoic (2.45–2.20 Ga) magmatic activity during the period of global magmatic shutdown: Implications for the crustal evolution of the southern North China Craton, *Precambrian Res.*, 255, 627–640, <https://doi.org/10.1016/j.precamres.2014.08.001>, 2014.

Diwu, C. R., Liu, X., and Sun, Y.: The composition and evolution of the Taihua Complex in the southern North China Craton, *Acta Petrol. Sin.*, 34, 999–1018, 2018 (in Chinese with English abstract).

Fan, Y. H., Zhu, X. Y., Duan, Q. S., Ma, J. F., Jia, C. Y., Liu, S. Q., and Zhao, T. P.: Discovery of 1.79 Ga dacite porphyry in the Taiyueshan Mts: Constraints on the genesis of the southern rift system in the North China Craton, *Acta Petrologica Sinica*, 40, 1327–1342, <https://doi.org/10.18654/1000-0569/2024.04.17>, 2024 (in Chinese with English abstract).

Gao, J. F., Zhou, M. F., Robinson, P. T., Wang, C. Y., Zhao, J. H., and Malpas, J.: Magma mixing recorded by Sr isotopes of plagioclase from dacites of the Quaternary Tengchong volcanic field, SE Tibetan Plateau, *J. Asian Earth Sci.*, 98, 1–17, <https://doi.org/10.1016/j.jseae.2014.10.036>, 2015.

Geng, Y. S., Yang, C. H., and Wan, Y. S.: Paleoproterozoic granitic magmatism in Lüliang area, North China Craton: constraint from isotopic geochronology, *Acta Petrologica Sinica*, 22, 305–314, 2006 (in Chinese with English abstract).

Geng, Y. S., Du, L. L., and Ren, L. D.: Growth and reworking of the early Precambrian continental crust in the North China Craton: Constraints from zircon Hf isotopes, *Gondwana Res.*, 21, 517–529, <https://doi.org/10.1016/j.gr.2011.07.006>, 2012.

Gorton, M. P. and Schandl, E. S.: From continents to island arcs: A geochemical index of tectonic setting for arc-related and within-plate felsic to intermediate volcanic rocks, *Can. Mineral.*, 38, 1065–1073, <https://doi.org/10.2113/gscanmin.38.5.1065>, 2000.

Grimes, C. B., John, B. E., Kelemen, P. B., Mazdab, F., Wooden, J. L., Cheadle, M. J., Hanghøj, K., and Schwartz, J. J.: Trace element chemistry of zircons from oceanic crust: a method for distinguishing detrital zircon provenance, *Geology*, 35, 643–646, <https://doi.org/10.1130/G23603A.1>, 2007.

Hawkesworth, C. J., Norry, M. J., Roddick, J. C., Baker, P. E., Francis, P. W., and Thorpe, R. S.: $^{143}\text{Nd} / ^{144}\text{Nd}$, $^{87}\text{Sr} / ^{86}\text{Sr}$, and incompatible element variations in calc-alkaline andesites and plateau lavas from South America, *Earth Planet. Sci. Lett.*, 42, 45–57, [https://doi.org/10.1016/0012-821X\(79\)90189-4](https://doi.org/10.1016/0012-821X(79)90189-4), 1979.

Hawkesworth, C. J. and Kemp, A. I. S.: Using hafnium and oxygen isotopes in zircons to unravel the record of crustal evolution, *Chem. Geol.*, 226, 144–162, <https://doi.org/10.1016/j.chemgeo.2005.09.018>, 2006.

He, J., Qi, Y., Fan, X., and Chen, F.: Petrogenesis of the Taishanmiao A-type granite in the eastern Qinling orogenic belt: Implications for tectonic transition and mineralization in the Late Cretaceous, *J. Geol.*, 129, 97–114, <https://doi.org/10.1086/713726>, 2021.

He, Y. H., Zhao, G. C., Sun, M., and Wilde, S. A.: Geochemistry, isotope systematics and petrogenesis of the volcanic rocks in the Zhongtiao Mountain: An alternative interpretation for the evolution of the southern margin of the North China Craton, *Lithos*, 102, 158–178, <https://doi.org/10.1016/j.lithos.2007.09.004>, 2008.

He, Y. H., Zhao, G. C., Sun, M., and Xia, X.: SHRIMP and LA-ICP-MS zircon geochronology of the Xiong'er volcanic rocks: Implications for the Paleo-Mesoproterozoic evolution of the southern margin of the North China Craton, *Precambrian Res.*, 168, 213–222, <https://doi.org/10.1016/j.precamres.2008.09.011>, 2009.

He, Y. H., Zhao, G. C., Sun, M., and Han, Y. G.: Petrogenesis and tectonic setting of volcanic rocks in the Xiaoshan and Waifangshan areas along the southern margin of the North China Craton: Constraints from bulk-rock geochemistry and Sr–Nd isotopic composition, *Lithos*, 114, 186–199, <https://doi.org/10.1016/j.lithos.2009.08.008>, 2010.

Hickey, R. L. and Frey, F. A.: Geochemical characteristics of boninite series volcanics: implications for their source, *Geochim. Cosmochim. Acta*, 46, 2099–2115, [https://doi.org/10.1016/0016-7037\(82\)90188-0](https://doi.org/10.1016/0016-7037(82)90188-0), 1982.

HIGS (Henan Institute of Geological Survey): Sheet I-49-(23) (Lushan) scale 1:200 000 geological map of the Henan Province. Bureau of Geology and Mineral Resources of Henan Province, Zhengzhou, Henan, Map, 2001 (in Chinese).

Hou, G. T., Li, J. H., Yang, M. H., Yao, W. H., Wang, C. C., and Wang, Y. X.: Geochemical constraints on the tectonic environment of the Late Paleoproterozoic mafic dyke swarms in the North China Craton, *Gondwana Res.*, 13, 103–116, <https://doi.org/10.1016/j.gr.2007.06.005>, 2008.

Hoskin, P. W. O., Kinny, P. D., Wyborn, D., and Chappell, B. W.: Identifying accessory mineral saturation during differentiation in granitoid magmas: an integrated approach, *J. Petrol.*, 41, 1365–1396, <https://doi.org/10.1093/petrology/41.9.1365>, 2000.

Hu, G. H., Hu, J. L., Chen, W., and Zhao, T. P.: Geochemistry and tectonic setting of the 1.78 Ga mafic dyke swarms in the Mt. Zhongtiao and Mt. Song areas, the southern margin of the North China Craton, *Acta Petrologica Sinica*, 26, 1563–1576, 2010 (in Chinese with English abstract).

Hu, G. Y., Zeng, L. S., Gao, L. E., Liu, Q. P., Chen, H., and Guo, Y. S.: Diverse magma sources for the Himalayan leucogranites: Evidence from B–Sr–Nd isotopes, *Lithos*, 314/315, 88–99, <https://doi.org/10.1016/j.lithos.2018.05.022>, 2018.

Huang, X. L., Xu, Y. G., and Liu, D. Y.: Geochronology, petrology and geochemistry of the granulite xenoliths from Nushan, east China: implication for a heterogeneous lower crust beneath the Sino-Korean Craton, *Geochim. Cosmochim. Acta*, 68, 127–149, [https://doi.org/10.1016/S0016-7037\(03\)00416-2](https://doi.org/10.1016/S0016-7037(03)00416-2), 2004.

Jackson, M. D., Cheadle, M. J., and Atherton, M. P.: Quantitative modeling of granitic melt generation and segregation in the continental crust, *J. Geophys. Res.-Sol. Ea.*, 108, 2332, <https://doi.org/10.1029/2001JB001050>, 2003.

Jia, C. Z.: Petro-geochemistry of volcanic rocks in the Xiong'er Group: implications for tectonic setting, *Henan Geol.*, 2, 39–43 (in Chinese with English abstract), 1985.

Jochum, K. P., Seufert, H. M., Spettel, B., and Palme, H.: The solar-system abundances of Nb, Ta, and Y, and the relative abundances of refractory lithophile elements in differentiated planetary bodies, *Geochim. Cosmochim. Acta*, 50, 1173–1183, [https://doi.org/10.1016/0016-7037\(86\)90400-X](https://doi.org/10.1016/0016-7037(86)90400-X), 1986.

Kelemen, P. B.: Genesis of high Mg[#] andesites and the continental crust, *Contrib. Mineral. Petrol.*, 120, 1–19, <https://doi.org/10.1007/BF00311004>, 1995.

Kröner, A., Compston, W., Zhang, G.-W., Guo, A.-L., and Todt, W.: Age and tectonic setting of Late Archean greenstone-gneiss terrain in Henan Province, China, as revealed by single-grain zircon dating, *Geology*, 16, 211–215, [https://doi.org/10.1130/0091-7613\(1988\)016<0211:AATSOL>2.3.CO;2](https://doi.org/10.1130/0091-7613(1988)016<0211:AATSOL>2.3.CO;2), 1988.

Le Bas, M. J., Le Maitre, R. W., Streckeisen, A., and Zanettin, B.: A Chemical Classification of Volcanic-Rocks Based on the Total Alkali Silica Diagram, *J. Petrol.*, 27, 745–750, <https://doi.org/10.1093/petrology/27.3.745>, 1986.

Li, X. P., Yang, Z. Y., Zhao, G. C., Grapes, R., and Guo, J. H.: Geochronology of khondalite-series rocks of the Jining Complex: Confirmation of depositional age and tectonometamorphic evolution of the North China craton, *Int. Geol. Rev.*, 53, 1194–1211, <https://doi.org/10.1080/00206810903548984>, 2011.

Liu, A. L., Hai, L. F., Liu, J. K., Zhang X. J., Li H. F., Zhao F. S., Zhao G. L., and Bai J. H.: Geochronology, Geochemistry, and Sr–Nd–Hf Isotopes of the Diorite Porphyrites from the Weining Beishan Area, Ningxia Hui Autonomous Region: Constraints on Their Source and Tectonic Implications, *J. Earth Sci.*, 35, 462–475, <https://doi.org/10.1007/s12583-021-1491-2>, 2024.

Liu, D. Y., Nutman, A. P., Compston, W., Wu, J. S., and Shen, Q. H.: Remnants of ≥ 3800 Ma crust in the Chinese part of the Sino-Korean Craton, *Geology*, 20, 339–342, [https://doi.org/10.1130/0091-7613\(1992\)020<0339:ROMCIT>2.3.CO;2](https://doi.org/10.1130/0091-7613(1992)020<0339:ROMCIT>2.3.CO;2), 1992.

Liu, Y. S., Hu, Z. C., Zong, K. Q., Gao, C. G., Gao, S., Xu, J. A., and Chen, H. H.: Reappraisal and refinement of zircon U–Pb isotope and trace element analyses by LA-ICP-MS, *Chin. Sci. Bull.*, 55, 1535–1546, <https://doi.org/10.1007/s11434-010-3052-4>, 2010 (in Chinese with English abstract).

Lu, S. N., Zhao, G. C., Wang, H. C., and Hao, G. J.: Precambrian metamorphic basement and sedimentary cover of the North China Craton: A review, *Precambrian Res.*, 160, 77–93, 2008.

Luo, Y., Sun, M., Zhao, G. C., Li, S. Z., Xu, P., Ye, K., and Xia, X. P.: LA-ICP-MS U–Pb zircon ages of the Liaohe Group in the Eastern Block of the North China Craton: constraints on the evolution of the Jiao-Liao-Ji Belt, *Precambrian Res.*, 134, 349–371, <https://doi.org/10.1016/j.precamres.2004.07.002>, 2004.

Ma, J. F., Qu, C. H., Zhou, Y. Y., and Zhao, T. P.: The genesis of ca. 1.78 Ga granitoids in the Xiong'er large igneous province: Implications for continental crust generation, *Geol. Soc. Am. Bull.*, 135, 3213–3227, <https://doi.org/10.1130/B36694.1>, 2023a.

Ma, J. F., Wang, X. L., Yang, A. Y., and Zhao, T. P.: Tracking crystal-melt segregation and accumulation in the intermediate magma reservoir, *Geophys. Res. Lett.*, 50, e2022GL102540, <https://doi.org/10.1029/2022GL102540>, 2023b.

Maniar, P. D. and Piccoli, P. M.: Tectonic discrimination of granitoids, *Geol. Soc. Am. Bull.*, 101, 635–643, [https://doi.org/10.1130/0016-7606\(1989\)101<0635:TDOG>2.3.CO;2](https://doi.org/10.1130/0016-7606(1989)101<0635:TDOG>2.3.CO;2), 1989.

Pan, Z. J., Zhang, Q., Chen, G., Jiao, S. T., Du, X. L., Miao, X. Q., Wang, J. R., and An, Y.: Relation between Mesozoic magmatism and plate subduction in eastern China: Comparison among

Zhejiang-Fujian, Japan arc and Andes arc, *Acta Petrol. Sin.*, 33, 1507–1523, 2017 (in Chinese with English abstract).

Peacock, S. M., Rushmer, T., and Thompson, A. B.: Partial melting of subducting oceanic crust, *Earth Planet. Sc. Lett.*, 121, 227–244, [https://doi.org/10.1016/0012-821X\(94\)90042-6](https://doi.org/10.1016/0012-821X(94)90042-6), 1994.

Pearce, J. A.: Role of the sub-continental lithosphere in magma genesis at active continental margins, in: *Continental Basalts and Mantle Xenoliths*, edited by: Hawkesworth, C. J. and Norry, M. J., Shiva Publishing Ltd., Nantwich, 230–249, ISBN: 978-0906812341, 1983.

Pearce, J. A. and Peate, D. W.: Tectonic implications of the composition of volcanic arc magmas, *Annu. Rev. Earth Planet. Sc.*, 23, 251–285, <https://doi.org/10.1146/annurev.ea.23.050195.001343>, 1995.

Peccerillo, A. and Taylor, S. R.: Geochemistry of Eocene calc-alkaline volcanic rocks from the Kastamonu area, northern Turkey, *Contrib. Mineral. Petrol.*, 58, 130–143, <https://doi.org/10.1007/BF00384745>, 1976.

Peng, P., Zhai, M. G., Zhang, H. F., Zhao, T. P., and Ni, Z. Y.: Geochemistry and geological significance of the 1.8 Ga mafic dyke swarms in the North China Craton: an example from the junction of Shanxi, Hebei and Inner Mongolia, *Acta Petrol. Sin.*, 20, 439–456, 2004 (in Chinese with English abstract).

Peng, P., Zhai, M. G., Guo, J. H., Kusky, T., and Zhao, T. P.: Nature of mantle source contributions and crystal differentiation in the petrogenesis of the 1.78 Ga mafic dykes in the central North China craton, *Gondwana Res.*, 12, 29–46, <https://doi.org/10.1016/j.gr.2006.10.022>, 2007.

Peng, P., Zhai, M. G., Ernst, R. E., Guo, J. H., Liu, F., and Hu, B.: A 1.78 Ga large igneous province in the North China craton: The Xiong'er Volcanic Province and the North China dyke swarm, *Lithos*, 101, 260–280, <https://doi.org/10.1016/j.lithos.2007.07.006>, 2008.

Petford, N. and Atherton, M.: Na-rich partial melts from newly underplated basaltic crust: the Cordillera Blanca Batholith, Peru. *J. Petrol.*, 37, 1491–1521, <https://doi.org/10.1093/petrology/37.6.1491>, 1996.

Rapp, R. P. and Watson, E. B.: Dehydration melting of metabasalt at 8–32 kbar: Implications for continental growth and crust-mantle recycling, *J. Petrol.*, 36, 891–931, <https://doi.org/10.1093/petrology/36.4.891>, 1995.

Reubi, O. and Blundy, J.: A dearth of intermediate melts at subduction zone volcanoes and the petrogenesis of arc andesites, *Nature*, 461, 1269–1273, <https://doi.org/10.1038/nature08510>, 2009.

Roberts, M. P. and Clemens, J. D.: Origin of high-potassium, calc-alkaline, I-type granitoids, *Geology*, 21, 825–828, [https://doi.org/10.1130/0091-7613\(1993\)021<0825:OOHPTA>2.3.CO;2](https://doi.org/10.1130/0091-7613(1993)021<0825:OOHPTA>2.3.CO;2), 1993.

Schulz, B., Klemd, R., and Brätz, H.: Host rock compositional controls on zircon trace element signatures in metabasites from the Austroalpine basement, *Geochim. Cosmochim. Acta*, 70, 697–710, <https://doi.org/10.1016/j.gca.2005.10.001>, 2006.

Shannon, R. D.: Revised effective ionic-radii and systematic studies of interatomic distances in halides and chalcogenides, *Acta Crystallogr. A*, 32, 751–767, <https://doi.org/10.1107/S0567739476001551>, 1976.

Shen, F. N.: The discovery of unconformity within the Taihua Group and definition of its stratigraphic sequence in the Lushan area, Henan. *Reg. Geol. China*, 2, 135–140, 1994 (in Chinese with English abstract).

Siebel, W., Reitter, E., Wenzel, T., and Blaha U.: Sr isotope systematics of K-feldspars in plutonic rocks revealed by the Rb-Sr microdrilling technique, *Chem. Geol.*, 222, 183–199, <https://doi.org/10.1016/j.chemgeo.2005.06.012>, 2005.

Stern, C. and Kilian, R.: Role of the subducted slab, mantle wedge and continental crust in the generation of adakites from the Andean Austral Volcanic Zone, *Contrib. Mineral. Petrol.*, 123, 263–281, <https://doi.org/10.1007/s004100050155>, 1996.

Streck, M. J., Leeman, W. P., and Chesley, J.: High-magnesian andesite from Mount Shasta: A product of magma mixing and contamination, not a primitive mantle melt, *Geology*, 35, 351–354, <https://doi.org/10.1130/G23286A.1>, 2007.

Sun, Q. Y., Zhou, Y. Y., Wang, W., Li, C. D., and Zhao, T. P.: Formation and evolution of the Paleoproterozoic meta-mafic and associated supracrustal rocks from the Lushan Taihua Complex, southern North China Craton: Insights from zircon U-Pb geochronology and whole-rock geochemistry, *Precambrian Res.*, 303, 428–444, <https://doi.org/10.1016/j.precamres.2017.05.018>, 2017.

Sun, S. S. and McDonough, W. F.: Chemical and isotopic systematics of oceanic basalts: implications for mantle composition and processes, *Geol. Soc. Lon. Spec. Publ.*, 42, 313–345, <https://doi.org/10.1144/GSL.SP.1989.042.01.19>, 1989.

Vermeesch, P.: IsoplotR: A free and open toolbox for geochronology, *Geoscience Frontiers*, 9, 1479–1493, <https://doi.org/10.1016/j.gsf.2018.04.001>, 2018.

Wan, Y. S., Wlide, S., Liu, D. Y., Yang, C. X., Song, B., and Yin, X. Y.: Further evidence for ~1.85 Ga metamorphism in the Central Zone of the North China Craton: SHRIMP U-Pb dating of zircon from metamorphic rocks in the Lushan area, Henan Province, *Gondwana Res.*, 9, 189–197, <https://doi.org/10.1016/j.gr.2005.06.010>, 2006.

Wang, C. M., Lu, Y. J., He, X. Y., Wang, Q. H., and Zhang, J.: The Paleoproterozoic diorite dykes in the southern margin of the North China Craton: Insight into rift-related magmatism, *Precambrian Res.*, 277, 26–46, <https://doi.org/10.1016/j.precamres.2016.02.009>, 2016.

Wang, J. L., Zhang, H. F., Zhang, J., Santosh, M., and Bao, Z. A.: Highly heterogeneous Pb isotope composition in the Archean continental lower crust: Insights from the high-grade metamorphic suite of the Taihua Group, Southern North China Craton, *Precambrian Res.*, 350, 105927, <https://doi.org/10.1016/j.precamres.2020.105927>, 2020.

Wang, M. X., Wang Z. Y., Zhao J. X., Qi, Z. Q., He, J., and Chen, F. K.: Petrogenesis and Geologic Implication of the Late Paleoproterozoic A-type Xiaohuo Pluton along the Southern Margin of the North China Craton, *Geol. J. China Univ.*, 29, 809–830, 2023a (in Chinese with English abstract).

Wang, X., Zhu, W., Luo, M., Ren, X., and Cui, X.: Approximately 1.78 Ga mafic dykes in the Lüliang Complex, North China Craton: Zircon ages and Lu-Hf isotopes, geochemistry, and implications, *Geochem. Geophys. Geosy.*, 15, 3123–3144, <https://doi.org/10.1002/2014GC005378>, 2014.

Wang, X., Huang, X., and Yang, F.: Revisiting the Lushan-Taihua Complex: New perspectives on the Late Mesoarchean-Early Neoarchean crustal evolution of the southern

North China Craton, *Precambrian Res.*, 325, 132–149, <https://doi.org/10.1016/j.precamres.2019.02.020>, 2019.

Wang, X. L., Jiang, S. Y., and Dai, B. Z.: Melting of enriched Archean subcontinental lithospheric mantle: Evidence from the ca. 1760 Ma volcanic rocks of the Xiong'er Group, southern margin of the North China Craton, *Precambrian Res.*, 182, 204–216, <https://doi.org/10.1016/j.precamres.2010.08.007>, 2010.

Wang, Y., Zhao, G., Cawood, P. A., Fan, W., Peng, T., and Sun, L.: Geochemistry of Paleoproterozoic (~1770 Ma) mafic dikes from the Trans-North China Orogen and tectonic implications, *J. Asian Earth Sci.*, 33, 61–77, <https://doi.org/10.1016/j.jseaes.2007.10.018>, 2008.

Wang, Y. J., Fan, W. M., Zhang, Y., Guo, F., Zhang, H., and Peng, T.: Geochemical, 40Ar/39Ar geochronological and Sr-Nd isotopic constraints on the origin of Paleoproterozoic mafic dikes from the southern Taihang Mountains and implications for the ca. 1800 Ma event of the North China Craton, *Precambrian Res.*, 135, 55–77, <https://doi.org/10.1016/j.precamres.2004.07.005>, 2004.

Wang, Z. Y., Cheng, H., Zhao, J. X., Ye, R. S., Li, W. Y., He, J. F., and Chen, F. K.: Sr-Nd-Pb isotopic composition of the Chinese national standard igneous rock powders measured by thermal ionization mass spectrometry, *Geol. J. China Univ.*, 29, 679–692, 2023b (in Chinese with English abstract).

Wang, Z. Y., Zhao, J. X., Qi, Z. Q., Huo, D. Y., Siebel, W., He, J., Li, S. Q., and Chen, F. C.: Two stages of late Paleoproterozoic A-type granites at the southern North China Craton: Geochemical constraints and implications for supercontinent breakup, *Precambrian Research*, 411, 107500, <https://doi.org/10.1016/j.precamres.2024.107500>, 2024.

Wolf, M., Romer, R. L., and Glodny, J.: Isotope disequilibrium during partial melting of metasedimentary rocks, *Geochim. Cosmochim. Acta*, 257, 163–183, <https://doi.org/10.1016/j.gca.2019.05.008>, 2019.

Wolf, M. B. and Wyllie, P. J.: Garnet growth during amphibolite anatexis: Implications of a garnetiferous restite, *J. Geol.*, 101, 357–373, <https://doi.org/10.1086/648229>, 1993.

Xu, J. H., Jiang, Y. P., Hu, S. L., Zhang, Z. W., Wu, C. Q., Zheng, C. F., Li, X. Y., Jin, Z. R., Zhang, S. S., and Zhou, Y. T.: Petrogenesis and Tectonic Implications of the Paleoproterozoic A-Type Granites in the Xiong'ershan Area along the Southern Margin of the North China Craton, *J. Earth Sci.*, 35, 416–429, <https://doi.org/10.1007/s12583-021-1424-0>, 2024.

Xu, Y. H., Zhao, T. P., Zhang, Y. X., and Chen, W.: Geochemical characteristics and geological significance of the detrital rocks from the Dagushi Formation of the Paleoproterozoic Xiong'er Group in the southern North China Craton, *Geological Review*, 54, 316–326, <https://doi.org/10.3321/j.issn:0371-5736.2008.03.004>, 2008.

Xue, L. W., Yuan, Z. L., Zhang, M. S., and Qiang, L. Z.: The Sm-Nd isotope ages of Tai-hua Group in the Lushan area and their implications, *Geochimica*, 24, 92–97, 1995 (in Chinese with English abstract).

Yang, J. H., Cawood, P. A., Du, Y. S., Huang, H., Huang, H. W., and Tao, P.: Large Igneous Province and magmatic arc sourced Permian–Triassic volcanicogenic sediments in China, *Sedimentary Geol.*, 261/262, 120–131, <https://doi.org/10.1016/j.sedgeo.2012.03.018>, 2012.

Yang, Z. M., Lu, Y. J., Hou, Z. Q., and Chang, Z. S.: High-Mg diorite from Qulong in southern Tibet: implications for the genesis of adakite-like intrusions and associated porphyry Cu deposits in collisional orogens, *J. Petrol.*, 56, 227–254, <https://doi.org/10.1093/petrology/egu076>, 2015.

Zeng, L. S., Asimow, P. D., and Saleeby, J. B.: Coupling of anatetic reactions and dissolution of accessory phases and the Sr and Nd isotope systematics of anatetic melts from a metasedimentary source, *Geochim. Cosmochim. Acta*, 69, 3671–3682, <https://doi.org/10.1016/j.gca.2005.02.035>, 2005.

Zhai, M. G.: Tectonic evolution and metallogenesis of North China Craton, *Mineral Deposits*, 29, 24–36, 2010 (in Chinese with English abstract).

Zhai, M. G.: Cratonization and the Ancient North China Continent: A summary and review, *Sci China Earth Sci.*, 54, 1110–1120, <https://doi.org/10.1007/s11430-011-4250-x>, 2011 (in Chinese with English abstract).

Zhao, G. C. and Zhai, M. G.: Lithotectonic elements of Precambrian basement in the North China Craton: Review and tectonic implications, *Gondwana Res.*, 23, 1207–1240, <https://doi.org/10.1016/j.gr.2012.08.016>, 2013.

Zhao, G. C., Cawood, P. A., Wilde, S. A., Min, S., and Lu, L. Z.: Metamorphism of basement rocks in the Central Zone of the North China Craton: implications for Paleoproterozoic tectonic evolution, *Precambrian Res.*, 103, 55–88, [https://doi.org/10.1016/S0301-9268\(00\)00076-0](https://doi.org/10.1016/S0301-9268(00)00076-0), 2000a.

Zhao, G. C., Wilde, S. A., Cawood, P. A., and Lu, L. Z.: Petrology and P-T path of the Fuping mafic granulites: implications for tectonic evolution of the central zone of the North China Craton, *J. Metamorphic Geol.*, 18, 375–391, <https://doi.org/10.1046/j.1525-1314.2000.00264.x>, 2000b.

Zhao, G. C., Wilde, S. A., Cawood, P. A., and Sun, M.: Archean blocks and their boundaries in the North China Craton: lithological, geochemical, structural and P-T path constraints and tectonic evolution, *Precambrian Res.*, 107, 45–73, [https://doi.org/10.1016/S0301-9268\(00\)00154-6](https://doi.org/10.1016/S0301-9268(00)00154-6), 2001.

Zhao, G. C., Sun, M., Wilde, S. A., and Li Sanzhong.: Late Archean to Paleoproterozoic evolution of the North China Craton: key issues revisited. *Precambrian Res.*, 136, 177–202, <https://doi.org/10.1016/j.precamres.2004.10.002>, 2005.

Zhao, G. C., Wilde, S. A., Sun, M., Li, S., Li, X., and Zhang, J.: SHRIMP U–Pb zircon ages of granitoid rocks in the Lüliang Complex: Implications for the accretion and evolution of the Trans-North China Orogen, *Precambrian Research*, 160, 213–226, <https://doi.org/10.1016/j.precamres.2007.07.004>, 2008.

Zhao, G. C., He, Y. H., and Sun, M.: Xiong'er volcanic belt at the North China Craton: The Xiong'er volcanic belt at the southern margin of the North China Craton: Petrographic and geochemical evidence for its outboard position in the Paleo-Mesoproterozoic Columbia Supercontinent, *Gondwana Res.*, 16, 170–181, <https://doi.org/10.1016/j.gr.2009.02.004>, 2009.

Zhao, J., Zhang, C., Guo, X., and Liu, X.: The late-Paleoproterozoic I- and A-type granites in Lüliang Complex, North China Craton: New evidence on post-collisional extension of Trans-North China Orogen, *Precambrian Research*, 318, 70–88, <https://doi.org/10.1016/j.precamres.2018.09.007>, 2018.

Zhao, T. P.: The characteristic and genesis of Proterozoic potassic volcanic rock in southern margin of the North plate, Doc-

toral dissertation, Institute of Geology and Geophysics, Chinese Academy of Sciences, Beijing, 102 pp., 2000.

Zhao, T. P., Xu, Y. H., and Zhai, M. G.: Petrogenesis and tectonic setting of the Paleoproterozoic Xiong'er Group in the southern part of the North China Craton: A review, *Geol. J. China Univ.*, 13, 191–206, 2007 (in Chinese with English abstract).

Zhao, T. P., Zhou, M. F., Zhai, M. G., and Xia, B.: Paleoproterozoic rift-related volcanism of the Xiong'er Group, North China Craton: Implications for the breakup of Columbia, *Int. Geol. Rev.*, 44, 336–351, <https://doi.org/10.2747/0020-6814.44.4.336>, 2002.

Zhao, T. P., Zhai, M. G., Xia, B., Li, H. M., and Zhang, Y. X.: Zircon U-Pb SHRIMP dating for the volcanic rocks of the Xiong'er Group: Constraints on the initial formation age of the cover of the North China Craton, *Chin. Sci. Bull.*, 49, 2495–2502, 2004 (in Chinese with English abstract).

Zhang, G. W., Bai, Y. B., Sun, Y., Guo, A. L., Zhou, D. W., and Li, T. H.: Composition and evolution of the Archaean crust in central Henan, China, *Precambrian Res.*, 27, 7–35, [https://doi.org/10.1016/0301-9268\(85\)90004-X](https://doi.org/10.1016/0301-9268(85)90004-X), 1985.

Zou, X. Y., Qin, K. Z., Han, X. L., Li, G. M., Evans, N. J., Li, Z. Z., and Yang, W.: Insight into zircon REE oxy-barometers: A lattice strain model perspective, *Earth Planet. Sc. Lett.*, 506, 87–96, <https://doi.org/10.1016/j.epsl.2018.10.031>, 2019.